This is a preprint, the final version is subject to change, of the American Mineralogist (MSA)
Cite as Authors (Year) Title. American Mineralogist, in press.
(DOI will not work until issue is live.) DOI: http://dx.doi.org/10.2138/am-2016-5776

Experimental evidence of the formation of intermediate phases during transition of kaolinite into metakaolinite

Revision 1

Victor A. Drits [1]*, Arkadiusz Derkowski [2], Boris A. Sakharov [1], and Bella B. Zviagina [1]

[1] Geological Institute of the Russian Academy of Science, Pyzhevsky per. 7, 119017 Moscow, Russia

[2] Institute of Geological Sciences, Polish Academy of Sciences, Senacka 1, 31-002 Krakow, Poland

* corresponding author; e-mail: victor.drits@mail.ru

Abstract

The phase composition of partially dehydroxylated specimens of two Clay Mineral Society standards, named KGa-1 and KGa-2 samples, were studied by powder X-ray diffraction patterns (XRD), infrared (IR) spectroscopy, and thermogravimetric (TG) data. Each specimen was preheated during 6h in isothermal conditions, and the heating temperatures were selected to cover the entire range of dehydroxylation for both kaolinites (380-550°C for KGa-2 and 400-600°C for KGa-1). Products preheated at 550°C and 600°C are named metakaolinite, as their XRD patterns showed no traces of kaolinite reflections. The contribution of metakaolinite to the experimental XRD pattern and IR spectrum of each preheated specimen (including 3550-3750 and 500-1300 cm^{-1} ranges) was determined by the simulation of the experimental pattern with a sum of the XRD patterns or IR spectra corresponding to the untreated sample and metakaolinite. This procedure showed that the contents of metakaolinite determined independently by diffraction and spectroscopic methods for each of the preheated specimen have almost identical values. Although the modeled and experimental XRD and IR spectra generally match, they contain particular ranges where the intensity differences are particularly significant. The misfits suggest the presence of a third phase forming in partially dehydroxylated kaolinite. To reveal the diffraction and spectroscopic features

of the kaolinite and possible intermediate phase (or phases), the contribution of metakaolinite was subtracted from the experimental XRD pattern and diffuse reflectance infrared Fourier transform(DRIFT) spectrum of each preheated specimen. Analysis of the metakaolinite-free XRD patterns and DRIFT spectra supports the idea that each preheated specimen, along with metakaolinite and initial kaolinite, contains a kaolinite-like component termed the intermediate phase. To determine the contents and specific diffraction features of the intermediate phases, the contribution of initial, untreated kaolinite was subtracted from the metakaolinite-free XRD patterns for each preheated specimen. In both samples, the content of the intermediate phase, $C_{inter,}$ decreases with the growth of metakaolinite from 23-25% at the beginning of dehydroxylation to 2% when the XRD-determined content of metakaolinite is 98%.The analysis of the diffraction features of the intermediate phases formed during partial dehydroxylation of the KGa-1 and KGa-2 samples indicates that they represent a new type of defective kaolinite-like structure, in which, along with the one-dimensional periodicity along the c* axis and the layer displacement vectors typical for natural kaolinite samples, the octahedral sheets of the individual layers of the structure are partially dehydroxylated.

Key words: kaolinite, metakaolinite, dehydroxylation, X-ray diffraction, infrared spectroscopy, thermogravimetry

Introduction

Kaolinite is a natural clay mineral, which occurs in various geological environments and has various industrial applications that require its prior thermal treatment. Comprehensive studies to gain insight into the mechanism of structural transformations of kaolinite governed by the dehydroxylation reaction have been conducted for decades. Notably, Suitch (1986) studied the mechanism of dehydroxylation of the Keokuk (highly ordered) kaolinite sample using powder X-ray diffraction (XRD) and Rietveld refinement method. When dehydroxylated up to 40% after heating at 425°C the individual crystallites forming the sample either completely altered to form metakaolinite, or retained all structural details of the unheated sample. Following that finding, many other experimental techniques were used to characterize the transition of kaolinite into metakaolinite: magic angle spinning nuclear magnetic resonance (MAS NMR; MacKenzie et al., 1983; Rocha and Kalinowski, 1990;Massiot et al., 1995;Rocha, 1999; He et al., 2003; Paris, 2014), infrared spectroscopy (IR; Frost et al., 1995, Frost and Vassallo,1995; Brindley et al.,1986), thermal analysis methods (Yeskin et al.,1985; Guggenheim and Van Gross, 1992, 2001; Dion et al., 1998; Ptacek et al., 2011; Drits and Derkowski, 2015), electron paramagnetic resonance (EPR; Djemai et al., 2001), transmission electron microscopy (TEM; Bergaya et al., 1996; Lee et al., 1999). Application of these techniques provided significant insight into the local atomic structure of partially dehydoxylated kaolinite samples. Until now, however, it has been commonly accepted that partially dehydroxylated kaolinite consists of a physical mixture of two phases: initial, non-dehydroxylated kaolinite and metakaolinite.

White et al. (2010a,b) emphasized that determination of partially dehydroxylated kaolinite structures by the conventional techniques does not provide thermodynamic information needed to ensure plausibility of these structures. These authors developed a new approach where the kaolinite dehydroxylation reaction was modeled using the density functional theory (DFT), and a step-wise protocol, where portions of water molecules were progressively removed from the structure with subsequent geometry optimization. The structure thus remained in a chemically, energetically, and

thermodynamically feasible state while the transition from kaolinite to metakaolinite was found to occur through partially dehydroxylated phases. Thirteen intermediate structures were simulated in the course of the structural evolution of the partially dehydroxylated kaolinite. For these simulated structures, neutron and X-ray pair distribution functions were generated and compared with the experimental patterns obtained for the KGa-1b kaolinite sample preheated at different temperatures. Close match between the simulated and experimental distribution functions proved the validity of the modeled intermediate structures (White et al., 2010a,b).

Using molecular dynamics Sperinck et al. (2011) simulated the thermally introduced transformation of kaolinite into metakaolinite through a set of partially dehydroxylated structures. These authors found that, during a step-wise dehydroxylation, Al cations migrate from the initial positions in the octahedral sheets of the kaolinite layers into interlayer sites to form 4- and 5-fold coordination of Al and causing a significant deformation of the layer structure. Therefore, according to White et al.(2010 a,b) and Sperinck et al.(2011), one pathway of dehydroxylation consists in the formation of chemically, energetically, and thermodynamically plausible intermediate structures of kaolinite, occurring at different stages of its dehydroxylation. If the conclusions of White et al. (2010a,b) and Sperinck et al.(2011) are correct, any partially dehydroxylated kaolinite sample will consist of a physical mixture of the initial kaolinite, metakaolinite, and a phase, whose structural and diffraction features are intermediate between these two phases.

The main objective of the present paper has been to reveal the actual phase composition of partially dehydroxylated kaolinite specimens based on the original methodological approaches and detailed analysis of powder X-ray diffraction patterns, infrared spectra, and thermogravimetrical (TG) data.

Kaolinite structure: theoretical background

Kaolinite, $Si_4Al_4O_{10}(OH)_8$, is a common dioctahedral 1:1 layer mineral. An individual kaolinite layer consists of one alumina octahedral sheet and one silica tetrahedral sheet that are bound to each other through apical oxygen atoms. Three symmetrically independent basal OH groups are referred to as surface OH because they form the outer basal surface of each layer. Hydrogen bonds between these OH groups and the basal oxygen atoms of the adjacent layer provide strong cohesion between layers. The fourth OH group is referred as inner OH because it is located within the layer. The octahedral sheet of the kaolinite layer contains three symmetrically independent sites differing in the arrangement of OH groups and oxygen atoms coordinating two octahedral Al cations and one vacant octahedron (Brindley and Robinson 1946). The kaolinite layer has a fixed chemical composition, with well-determined positions of each atom. However, the stacking pattern of adjacent layers produces a large variation of the kaolinite structures (Brindley et al. 1986; Bailey 1988). Bookin et al. (1989) showed that the diffraction features of a defect-free 1*Tc* kaolinite structure can be reproduced equally well by either of the layer displacement vectors $\mathbf{t_1}$ or $\mathbf{t_2}$, which correspond to the individual kaolinite enantiomorphs and are related to each other by the layer pseudo-mirror plane. Random interstratification of these vectors within individual kaolinite crystallites results in the interstratification of the right-hand and left-hand kaolinite subsequences of the same layer types thus producing most of the structural disorder in kaolinite. Because of the nearly trigonal symmetry of the kaolinite layer, the third layer displacement vector, $\mathbf{t_0}$, located along the pseudo-mirror plane may exist in the kaolinite structure. Therefore an accurate model of the defective kaolinite structure should be defined by the probability of t_1, t_2, and t_0 layer displacements, W_{t_1}, W_{t_2}, and W_{t_0}, respectively, which can be determined by the simulation of an experimental powder XRD pattern of a kaolinite sample (Bookin et al., 1989). The simulated interstratification of the right- and left-hand structural fragments in natural kaolinite samples from XRD is in agreement

with the results of high-resolution TEM (Kogure and Inoue, 2005; Kogure et al., 2010). Based on the above model, Plançonet al. (1989) simulated a set of the experimental XRD patterns of natural kaolinite samples and showed that, as a rule, they consist of a physical mixture of two distinct populations of kaolinite crystallites, one with a low-defect structure and the other with a moderate to high-defect structure.

Samples

Two Clay Minerals Society reference kaolinites, the KGa-2 sample with a low degree of structural order, and the so-called well-ordered KGa-1 sample, were used in this study. The actual structure of these samples was determined by the simulation of their powder XRD patterns using a model that provides the best possible agreement in the positions, intensities, and profiles of *hkl* reflections found between the calculated and the experimental XRD patterns by Sakharov et al. (2016). These authors simulated the diffraction effects using the refined atomic coordinates of Bish and von Dreele (1989) and a program of B. Sakharov and A. Naumov, based on algorithms of Drits and Tchoubar (1990). The same program and approach were used in this study to provide the best possible agreement between the experimental XRD pattern of a sample consisting of a mixture of two or three phases and an XRD pattern simulated as a sum of XRD patterns corresponding to these components. The contents of the component phases and their respective contributions to the bulk XRD patterns were assumed equal. The quality of the agreement between the experimental and the calculated XRD patterns was estimated by the profile factor, R_p, given by

$$R_p = \frac{\sum_i \left| I_i^{exp} - I_i^{calc} \right|}{\sum_i I_i^{exp}}$$

where I_i^{exp} and I_i^{calc} are the measured and calculated intensities, respectively, at each *i* step increment.

According to Sakharov et al. (2016), both studied samples consist of a high-ordered kaolinite (HOK) and low-ordered kaolinite (LOK) phases. In both samples, the HOK phase has an almost defect-free structure, where 97% layer pairs related by the layer displacement translation $\boldsymbol{t_1}$are randomly interstratified with only 3% layer pairs related by the translation $\boldsymbol{t_2}$. However, the content of the HOK phase is significantly higher in KGa-1 (24.3%) than in KGa-2 (3.9%). In the LOK phases, the layer displacement translations, t_1, t_2, and t_0 are interstratified at random in different proportions (Figure 1, Table 1). As shown in Figure 2 for the KGa-1 sample, despite a relatively low content of the HOK phase, it contributes significantly to the positions, widths, and intensities of 02*l*, 11*l* reflections, whereas the LOK crystallites contribute more to the background in a non-uniform manner and to the 020 reflection. The main feature of the XRD pattern of the KGa-1 sample is that the positions and relative intensity distribution of 11*l*, 02*l*, 20*l*, and 13*l* reflections are very close or almost identical to those in the XRD pattern of the 3D periodic one-layer triclinic kaolinite structure. For the same reason, the content of 3% of the t_2 layer displacement in the HOK phase could be reliably determined, because even a small increase in the t_2 content in the HOK structure shifts the positions of 11*l* and 02*l* reflections, which is easily monitored by XRD. In addition, the 20*l* and 13*l* reflections have almost the same positions in the XRD patterns of the HOK and LOK phases because they are fairly insensitive to the interstratification of the right- and left-hand kaolinite structural fragments (Sakharov et al., 2016). Different contents of the HOK phases in the studied samples are responsible for the substantial difference between their XRD patterns. In particular, the very low content of the HOK fraction in the KGa-2 sample minimizes the intensity of individual 11*l*, 02*l* reflections observed in the experimental XRD patterns (Figure 1).

The KGa-2 sample has a homogenous phase composition that is independent of the particle size fractions: particles of the same sizes have the same proportions of the HOK and LOK phases, and the same thermal evolution and XRD characteristics (Drits and Derkowski, 2015). KGa-1 has a bimodal particle size distribution with a coarser fraction of lower structural order albeit higher crystallite thickness and higher temperature of dehydroxylation, whereas the finer fraction has a

higher stacking order associated with thinner crystallites and lower temperature of dehydroxylation (Drits and Derkowski, 2015). Finally, the finer fraction of KGa-1 particles contains a higher proportion of the HOK phase as compared with that in the bulk sample. With increasing particle size the temperature required for dehydroxylation increases despite lower structural order.

Methods

Analytical methods

Powder X-ray diffraction (XRD) patterns of bulk samples were obtained with a D8 diffractometer (Bruker AXS GmbH, Germany). CuKα radiation and Ni-filter were used to record the randomized powder within 10-65°2θ range, with a step of 0.05°2θ, and irradiation time of 100 sec/step.

Infrared spectra (IR; 4000-580 cm^{-1}) were collected on an IR instrument Nicolet 6700 by Thermo Scientific, equipped with a Praying Mantis diffuse reflectance infrared Fourier transform (DRIFT) module by Harrick, using a sample mixed and ground with KBr powder in 5% ratio. The spectra are reported as 100-scan averages with 4 cm^{-1} resolution ($\Delta\nu$ = 2 cm^{-1} by interferogram zerofill). No instrumental or environmental correction was applied.

Thermogravimetric (TG) experiments were performed using the TA Discovery IR model thermal analyzer (TA Instruments) with a weighing error of < 1 μg, weight measurement resolution of < 0.1 μg, and a thermal drift between 200 and 1000°C of < 4 μg. A 20±0.5 mg sample was analyzed with a ramp heating from 25 to 1000°C, purged with dry N_2 gas of > 99.999% purity at a flow rate of 50 ml/min.

Ex-situ heating experiments

KGa-2 and KGa-1 bulk samples were used in the sequential heating experiments. Homogenized samples were split into twelve representative portions ~ 2g each. Each portion was loosely and equally spread thin with a smooth surface on a porcelain holder ~ 10 cm in diameter. A holder was placed in the center of a laboratory furnace with air circulation, pre-heated to a desired temperature. After 6 h of isothermal treatment, the holder was removed and the sample (still warm) was immediately transferred to a glass vial and sealed. The heating temperatures were selected to cover the entire range of dehydroxylation for both kaolinites (380-550°C for KGa-2 and 400-600°C for KGa-1). The partially dehydroxylated samples were then analyzed with TG as above to find their actual degree of dehydroxylation (D_T) by quantifying the mass loss of the non-dehydroxylated (residual OH) portion of the sample and to observe the shift of maximum DTG peak (cf. Drits et al., 2011a, b).

The D_T values for the preheated samples were determined independently using diffraction and spectroscopic methods, by comparing their experimental XRD patterns and DRIFT spectra to those calculated by linear mixing of the respective curves for a completely dehydroxylated (or assumed so) sample and the initial, non-dehydroxylated sample as end-members. Least-squares-based evolutionary optimization was applied to minimize the difference between the modeled and experimental patterns. In the DRIFT spectroscopy method, relative and absolute scaling was added to the mixed model to account for instrumental factors whereas in the XRD method the influence of instrumental factors was included directly into the calculation program in order to obtain absolute scaling of the pattern components.

Results

Thermogravimetry

The DTG pattern of KGa-2 sample has a near-symmetrical shape with a maximum (DTG_{max}) at 492°C, and a very broad high-temperature component ending at 750-800°C noticeable also in the

TG pattern. The KGa-1 sample has DTG_{max} at 512°C, a sharp, high-temperature component with a maximum at ~ 640°C, and a broad component ending at ~ 800°C (Figure 3, Table 2).

The TG patterns of partially dehydroxylated samples are qualitatively similar to those of the untreated samples. Total mass loss determined from the TG analysis between 300°C and 900°C was used to quantify the content of OH groups remaining in the partially dehydroxylated sample, which is the portion of the sample that was not dehydroxylated during ex-situ heating (Figure 3). The residual mass portion was subtracted from the mass loss determined in the untreated sample and normalized in order to determine the TG-measured degree of dehydroxylation, $D_T(TG)$. The mass loss of the untreated samples (13.7 % in both KGa-1 and KGa-2) closely matched the theoretical mass loss calculated from the mineral formulae, testifying to insignificantly low quantity of impurities in the samples (Table 2). Due to the high precision of the TG measurement the $D_T(TG)$ error is ± 0.5% absolute.

Increasing ex-situ heating temperature (T) increased the $D_T(TG)$ and the relationship of these parameters is far from linear. After the initial slow increase of $D_T(TG)$ with T, a rapid change occurs within only 10°C difference in T, reaching almost 30% of $D_T(TG)$ difference in KGa-1 and almost 40% in KGa-2 (Figure 3, Table 2). Then the $D_T(TG)$ increases more gently with T.

The variability of DTG_{max} with $D_T(TG)$ shows a spectacular pattern. In the KGa-2 DTG_{max} remains constant at 495±2°C through the first 26% of dehydroxylation, and increases only a little (to 502°C) at the $D_T(TG)$ = 65.5 %. Then the DTG_{max} increases abruptly at each higher T (Figure 4, Table 2). Similar evolution is observed for the KGa-1 sample, except for a gentle increase in DTG_{max}, which starts at $D_T(TG)$ = 15.4% and steepens after 65%. Moreover, the insignificant shift (if any) of DTG_{max} below $D_T(TG)$ ~ 70% seems to be produced by the increasing contribution from the high-temperature components rather than the actual shift of the peak corresponding to DTG_{max} of the untreated sample. The temperature range of DTG patterns of all partially dehydroxylated portions remain within the envelope of the untreated sample; as if only a portion of the initial

sample were completely dehydroxylated during the *ex-situ* heating while the remaining high-temperature components persisted unchanged.

DRIFT

Except for a few small but visible deviations, the DRIFT patterns of the *ex-situ* heated samples present a consistent step-wise pathway from an untreated kaolinite toward completely dehydroxylated structure (Figures 5 and 6). The OH-stretching at the 3550-3750 cm^{-1} range and OH-bending bands at ~ 915 and 936 cm^{-1} decrease linearly without changing their positions. The intensities of the bands at 696, 755, and ~ 790 cm^{-1} assigned by Frost et al. (1996) to "OH translational vibrations" and the intensities of the Si-O stretching bands at 1112, 1104, 1036, and 1012 cm^{-1} decrease with the progress of dehydroxylation. With increasing temperature of *ex-situ* heating the growth of the broad bands at 1076 and 1200 cm^{-1}, typical for amorphous silica, and the band at ~ 820 cm^{-1} assigned to tetrahedral Al (Rahier et al., 2000) was observed.

The linear mixing model of the untreated and completely dehydroxylated samples was used by simultaneously fitting two spectral ranges, 450-1300 cm^{-1} dominated by the Si-O vibrations and the OH bending modes and 3550-3750 cm^{-1} corresponding to the OH-stretching vibrations (Figures 5 and 6). The assumed completely dehydroxylated samples used as end-members for modeling were those heated at 550°C for KGa-2 and 600°C for KGa-1: these samples showed no traces of OH stretching bands, while in the range of 450-1300 cm^{-1} they did not show any features typical for untreated kaolinite. These dehydroxylated end-member samples were, however, not fully dehydroxylated in terms of TG; they both have $D_T(TG)$ of ~ 95% (Table 2). These specimens are considered to be pure metakaolinite containing residual H_2O. The D_T values calculated for partially dehydroxylated samples using DRIFT data, $D_T(IR)$, were reported as the percentage of the metakaolinite phase, uncorrected for the TG-determined D_T in the completely dehydroxylated end-members (Table 2, Figures 5 and 6). Testing the modeling by using different wavenumber ranges

and different fitting approaches revealed that the $D_T(IR)$ determination error is ±2%. The rate of conversion to metakaolinite was not linear with the preheating temperature: acceleration followed by deceleration (Table 2) matches the shape of the DTG curve (Figure 3).

Although the modeled and experimental spectra generally match, they contain particular ranges where the intensities of bands in the experimental spectra are lower than the corresponding bands in the modeled spectra (Figures 5, 6). The intensity difference is particularly significant for the bands assigned to one of the Si-O out-of-plane vibrations at ~ 1100 cm^{-1} and for the bending Al-OH bands at ~915 and ~937 cm^{-1}. To a lower extent, differences are observed for the OH stretching vibrations at 3620 cm^{-1} and 3656 cm^{-1}, and for the OH translational vibrations at ~ 790, ~750, and 698 cm^{-1}. In contrast, the intensity of octahedral Al vibrations at ~540 cm^{-1} decreased progressively with the preheating temperature (Figures 5 and 6).

XRD features

KGa-1 sample. Based on the XRD features, two groups of data can be distinguished based on the preheating temperature (Figure 7). In the specimens preheated at T ≤ 435°C the number and positions of the XRD reflections remain the same as those in the XRD pattern of the untreated sample.

The specimens preheated at T>435°C show variable features. In the diagnostic 2θ region, 19.0 - 27.0°, the intensities of the 02*l* and 11*l* reflections decrease progressively and finally become negligibly weak (Figure 7), implying that the initial kaolinite structure was subjected to certain structural rearrangements. The XRD pattern of the specimen preheated at 510°C demonstrates only weak but well-defined 001 (d(001) ~ 7.16Å) and 002 basal reflections, and a broad, asymmetrical maximum within 20-30°2θ (Figure 7). The specimen preheated at 600°C does show no XRD reflections of the initial kaolinite, so the pattern must correspond to metakaolinite (Figure 7). Along with the reflections of anatase, this pattern contains a broad, asymmetrical diffraction feature of

metakaolinite located at 20-30°2θ. Thus, the higher metakaolinite content in the specimens, the higher its contribution to the XRD pattern and the more noticeable the modification of the XRD pattern.

The optimized sum of end-members (initial kaolinite and metakaolinite produced by heating at 600°C) is in close agreement with the experimental patterns of preheated specimens (Figure 8). The most remarkable feature of the experimental and optimized XRD patterns corresponding to each preheating specimen is that the peak positions of the 02*l*, 11*l,* and 20*l*, 13*l* reflections coincide in both patterns. Certain discrepancies are observed consistently in the XRD regions between the 020 and ($1\bar{1}0$, 110), and between ($1\bar{1}0$, 110) and ($1\overline{11}$, $11\bar{1}$) reflections (19.9-20.4°2θ and 20.4-21.3°2θ, respectively; Figure 8). Because of these discrepancies, the profiles and intensities of the 020 and ($1\overline{11}$,$11\bar{1}$) reflections in the experimental and calculated XRD patterns only coincide along one slope of each reflection (see arrows in Figure 8). In the 20*l*, 13*l* region the reflection positions also coincide although the intensities of some of the compared reflections decrease (Figure 8). Except for the above XRD regions, the majority of the kaolinite XRD peaks in each preheated specimen coincide with those of the untreated sample. The misfits between the experimental and modeled patterns observed in the particular XRD regions suggest the presence of a third phase formed in the partially dehydroxylated kaolinite sample.

KGa-2 sample. The most significant modification in the XRD patterns of specimens preheated at different temperatures is observed in the 19.5-22.0°2θ region, where the intensity of the sharp 020 reflection decreases progressively with preheating temperature and becomes negligible at T> 430°C (Figure 7). The peak located close to the 020 reflection at 20.2°2θ shifts progressively to higher 2θ values and broadens consecutively (Figure 7). The evolution of the 20*l* and 13*l* reflections with increasing preheating temperature is similar to that observed for the KGa-1 sample (Figure 7). The shape of the broad, non-modulated maximum observed for the specimen preheated at 550°C is the

same as that in the XRD pattern of the KGa-1 sample preheated at 600°C (Figure 7), which implies that metakaolinite has the same or quite similar structure in both samples.

The experimental XRD patterns of the preheated KGa-2 specimens were simulated using the optimized sum of the XRD patterns of the initial sample and the specimen heated at 550°C (Figure 9). As in case of KGa-1, the most significant difference between the experimental and simulated patterns is observed in the 2θ range of 20-23°, where the intensity in the experimental XRD pattern is always higher than that in the simulated one (Figure 9). That gap increases with the metakaolinite content and reaches its maximum for the specimen preheated at 430°C ($D_T(XRD)$ = 78%). This is similar to the $D_T(XRD)$ value where the corresponding maximum discrepancy was observed in the KGa-1 sample. At the preheating temperature > 430°C, the gap decreased and the modeled and experimental patterns became similar (Figure 9).

Most importantly, the positions and intensities of basal reflections in the experimental and optimized XRD patterns coincide in each preheated specimen of both samples (Figures 8 and 9).The relative content of metakaolinite, assumed equal to the degree of dehydroxylation determined by XRD, increases from 20% at T = 425°C to 98% at T = 510°C for KGa-1 and from 5% at T = 410°C to 98% at T = 470°C for KGa-2 (Table 2). The degree of the conversion of kaolinite into metakaolinite does not depend linearly on the preheating temperature; instead, the relationship between $D_T(XRD)$ and T reflects the shape of the DTG curve (compare Table 2 and Figure 3).

Both KGa-1 and KGa-2 reference materials contain minor amounts of anatase, which becomes pronounced in the XRD patterns of specimens preheated at high temperatures (Figures7-9). Careful homogenization and splitting of the initial materials into representative portions allows assuming that the anatase content is the same in all preheated specimens of the sample studied, so that it can serve as an internal standard.

This is a preprint, the final version is subject to change, of the American Mineralogist (MSA)
Cite as Authors (Year) Title. American Mineralogist, in press.
(DOI will not work until issue is live.) DOI: http://dx.doi.org/10.2138/am-2016-5776

Discussion

Independent verification: kaolinite basal reflection intensity *vs.* $D_T(XRD)$

The XRD reflection intensity of mineral X, (I_X), and the intensity of the internal standard S, (I_S), in a XRD pattern of a bulk sample (minerals and the standard mixture) are

$I_X = \%C_X K_X \mu$ and $I_S = \%C_S K_S \mu$,

where μ is the mass absorption coefficient of the bulk sample; K_X and K_S are the constants for the chosen reflections of mineral X and standard S, respectively, dependent on their crystal structure, composition, density, and the XRD experimental conditions; $\%C_X$ and $\%C_S$ are the wt.% concentrations of X and S in a sample, respectively. For a set of specimens in which the wt.% of mineral X values varies within a certain range, whereas the standard content and μ remain the same, the ratio of I_X to I_S is proportional to the wt.% content of the mineral X in each of the studied specimens, so that

$$I_X/I_S = \%C_X K_X / \%C_S K_S = K\%C_X \quad (1)$$

Where K is the coefficient representing the experimental ratio K_X/K_S divided by C_S.

Following the above approach, the ratio of intensities of the 002 kaolinite (d = 3.578Å) and anatase (d = 3.520Å) reflections, I_{002}/I_{ant}, was measured from the XRD patterns of each preheated specimen of the KGa-1 and KGa-2 samples (Table 2). In the case of KGa-1 the I_{002}/I_{ant} ratio and $D_T(XRD)$ of the corresponding specimens are related by the linear regression

$$(I_{002}/I_{ant})_{KGa\text{-}1} = -0.1166 D_T(XRD)\% + 12.01 \quad R^2 = 0.991, \quad (2a)$$

while for the KGa-2 specimens, the regression returned the equation

$$(I_{002}/I_{ant})_{KGa\text{-}2} = -0.039 D_T(XRD)\% + 3.867 \quad R^2 = 0.996 \quad (2b)$$

shown in Figure10a by straight trend lines. Combining the relationships in Equations 2a and 2b with Equation 1, the coefficient K from Equation 1 is given by the intercept in Equation 2, while C_X from

Equation 1 is the kaolinite content (C_K). As a result, for the partially dehydroxylated KGa-1 specimens,

$(I_{002}/I_{ant})_{KGa\text{-}1} = 0.1201C_K = -0.1166D_T\ (XRD)\% + 12.01$, so that

$$\%C_K = 100 - 0.9709D_T(XRD) \quad (2c)$$

For the partially dehydroxylated KGa-2 specimens, we have

$(I_{002}/I_{ant})_{KGa\text{-}2} = 0.03867C_K = -0.039D_T(XRD)\% + 3.867$, so that

$$\%C_K = 100 - 1.0085D_T(XRD) \quad (2d)\ .$$

Equations 2c and 2d prove that an almost identical degree of dehydroxylation is derived using either the linear intensity variation of the 002 kaolinite reflection vs. anatase or the XRD simulation based on linear mixing of the metakaolinite and the initial kaolinite end-members in both KGa-1 and KGa-2 series. This agreement provides a cross-check confirmation that the XRD simulation method returns the true $D_T(XRD)$ value that is equal to the metakaolinite content.

Comparison of the degrees of dehydroxylation obtained using XRD, IR, and TG

Because the metakaolinite end-members used to calculate $D_T(XRD)$ and $D_T(IR)$ were not completely dehydroxylated in terms of $D_T(TG)$, in order to compare $D_T(TG)$ directly with $D_T(IR)$ and $D_T(XRD)$, the $D_T(TG)$ values were normalized under the assumption that the dehydroxylated end-members used for $D_T(XRD)$ and $D_T(IR)$ calculations have $D_T(TG)$=100%. These normalized $D_T(TG)$ values, $D_{Tn}(TG)$, were then used to obtain the linear relationships between the degrees of dehydroxylation determined with TG, XRD, and IR for the specimens of KGa-1 (Figures 10b-d) and for the specimens of the KGa-2 (Figures 10b-d).

These regressions show that the $D_T(XRD)$, $D_T(IR)$, and $D_{Tn}(TG)$ values obtained by three independent techniques are close to each other for each studied specimen. Certain deviations from

the ideal 1:1 correlation, however, occur consistently for both samples studied. As a rule, for low degrees of dehydroxylation, the $D_{Tn}(TG)$ values are equal to (in KGa-1) or higher (in KGa-2) than $D_T(XRD)$ and $D_T(IR)$, whereas approaching $D_T \approx 50\%$, $D_{Tn}(TG)$ becomes significantly lower than $D_T(XRD)$ and $D_T(IR)$. The values merge again at $D_T > 80\%$ (Figures 10c,d). In contrast, the $D_T(XRD)\%$ and $D_T(IR)\%$ values obtained for the same specimen are very similar and coincide within the experimental errors (Figure 10b), which cross-validates the methodology of $D_T(XRD)$ and $D_T(IR)$ determination by end-member patterns summation. For the KGa-2 specimens, the $D_T(XRD)$ values are, on average, systematically 2.4% higher than $D_T(IR)$, whereas in the KGa-1 specimens, the relationship is generally the opposite. Noticeably, in both the series studied, the highest mismatch between $D_T(XRD)$ and $D_T(IR)$, 4-5%, occurs in the same specimens that show the greatest excess of $D_T(XRD)$ and $D_T(IR)$ values over $D_{Tn}(TG)$ (Figure 10).

The difference between $D_T(IR)$ or $D_T(XRD)$ and $D_T(TG)$ reaches 16%, which is much greater than the values for the end-members used in the DRIFT fitting ($D_T(TG) \sim 95\%$; $D_T(IR) = 100\ \%$) (Table 2). Therefore, the excess of $D_T(IR)$ and $D_T(XRD)$ over $D_T(TG)$ is a real effect that does not result just from the lack of (or incorrect) normalization. Moreover, similar differences between $D_T(TG)$ and $D_T(IR)$ were observed by Rahier et al. (2000), who used intensities of particular bands to determine $D_T(IR)$. This discrepancy may have appeared when water pressure resulting from dehydroxylation of the octahedral sheet in the 1:1 layer was not high enough to induce the migration of H_2O molecules out of the crystallite or particle. The formed but not released H_2O molecules may have completely or partly dissociated within the interlayer or former octahedral sheet, leading to rehydroxylation. The degradation of OH-originated IR signal is caused by the distortion of OH groups linked to inhomogeneous Al environments of partially dehydroxylated-rehydroxylated layers leading to the loss of the IR signal coherency. Such structural transformations, however, would provide minimal contribution to the mass loss of the preheated specimens, resulting in the observed differences between $D_T(IR)$ or $D_T(XRD)$ and $D_{Tn}(TG)$.

Identification of the XRD features of the intermediate kaolinite-like phases

If the two-phase model of the preheated specimens were valid, the residual curve of the end-members summation would only consist of small intensity fluctuations originating from random errors of end-member content optimization. Instead, as shown in Figures 8 and 9, the differences are much greater than expected from the experimental errors. Moreover, the differential XRD features remain somehow consistent among specimens and samples. The features presented in the summation differential curves imply the presence of a phase different from the end-members.

Because the metakaolinite content is known and confirmed by the cross-validation of $D_T(XRD)$ and $D_T(IR)$, there is a chance to reveal the diffraction features of the kaolinite and the possible intermediate phase (or phases), which coexist with metakaolinite in each particular specimen. In order to do this, the contribution of metakaolinite equal to the $D_T(XRD)$ value was subtracted from the XRD pattern of each preheated specimen. The results of the subtraction shown in Figure 11, demonstrate the evolution of the metakaolinite-subtracted kaolinitic component with consecutive heating. If the two-phase composition model were correct, the absolute intensities of the *hkl* reflections in the XRD patterns would decrease consistently in accordance with the decrease in the initial kaolinite content, that is, with the $(100 - D_T(XRD))$ values. As expected from the summation differential curves (Figures 8 and 9), the metakaolinite-subtracted XRD patterns (Figure 11) contradict this interpretation. In particular, in the 19 - 24°2θ region the intensity distribution from the KGa-2 specimens preheated at 430 and 440°C differs significantly from that corresponding to the initial sample. Similarly, the distribution of intensities of the 20*l*, 13*l* region in the XRD patterns of the KGa-2 specimens differs substantially from that observed in the XRD pattern of the untreated sample (Figure 11).

In order to determine the content and diffraction features of the phases differing from the initial kaolinite, the contribution of initial kaolinite structure needed to be subtracted from the metakaolinite-subtracted XRD patterns produced during the previous subtraction step (Figure 11).

The second virtual subtraction was performed by the trial-and-error method, so as to avoid negative intensities in the resulting XRD pattern (cf. differential curves in Figures 8 and 9); that is, any portion of the differential curve was not to drop below zero. The resulting pattern is interpreted as corresponding to the intermediate phase of the particular specimen (Figure 12). The difference between the $C_K = (100 - D_T(XRD))$ value and the quantity of the subtracted initial kaolinite, C_{in}, thus corresponds to the fraction of the intermediate phase, C_{inter}, in the specimen (Table 2).

Reliability of the intermediate phases as seen by the DRIFT data

As in the case of XRD data, the model based on the initial kaolinite and final metakaolinite sum optimization does not match perfectly the experimental DRIFT spectra of preheated specimens. Differential spectra show consistent features with intensities much larger than fluctuations coming from experimental errors (Figures 5 and 6), suggesting the presence of another phase with vibrational characteristics differing from those of the end-members.

Following the procedure performed on XRD patterns of preheated specimens, metakaolinite contributions were subtracted separately from the bulk DRIFT spectra, based on the $D_T(IR)$ values. In both kaolinite samples the metakaolinite-subtracted spectra remain close to the initial kaolinite spectra up to the $D_T(IR)$ values of ~ 80%; then the band intensity distribution changes significantly in the 500-1300 cm^{-1} range (Figure 13).The OH-stretching bands become weaker, broader and all shift to higher wavenumbers, by 5-8 cm^{-1} in KGa-1 and only ~4 cm^{-1} in KGa-2. The resolution of the absorption bands at ~3652 and 3669 cm^{-1} is lost at $D_T(IR)$ >75% (Figure 13). It is unclear if the shift of OH-stretching bands originates from changes in the structure or results from dehydroxylating a portion of a sample containing OH groups with lower IR vibration frequencies than the average values.

A consistent series of IR bands not matching or not satisfied by the end-member contributions provide additional evidence of the presence of another component or several

components that can be considered intermediate, semi-dehydroxylated phases. The comparison of the metakaolinite-subtracted preheated specimens (Figure 13) suggests that the intermediate phase is included in the 100 – $D_T(IR)$ portion along with kaolinite. It is quite probable that the intermediate phase also evolves during heating or there is more than one intermediate phase formed at different degrees of dehydroxylation (cf. White et al., 2010 a,b).

The IR features of the intermediate phases become visible in the metakaolinite-subtracted spectra of the preheated specimens when the contents of the intermediate phases become similar to or greater than those of the remaining initial kaolinite (at T>450 and 430°C for samples KGa-1 and KGa-2, respectively, Table 2) (Figure 13). For example, in the spectra of sample KGa-1 preheated at 450°C and 460°C, the OH-stretching region displays kaolinite features, whereas all absorption bands below 900 cm^{-1} (OH-translational vibrations) are lost except the band at ~550 cm^{-1} (Si-O-Al bending). Moreover, the metakaolinite-subtracted spectrum of the KGa-1 specimen preheated at 510 cm^{-1}, which contains no initial kaolinite and only 2% of the intermediate phase (Table 2), shows no individual bands in the 500-1200 cm^{-1} range except two broad bands at ~1000 and 1200 cm^{-1} (Figure 13a). This spectrum differs substantially from that of metakaolinite and corresponds to the intermediate phase containing only a single feature of kaolinite, *i.e.* well-defined basal reflections (Figures 11 and 12). In contrast, in the metakaolinite-subtracted spectrum of sample KGa-2 preheated at T= 470°C, both OH-stretching and 500-1300 cm^{-1} regions do not contain any traces of kaolinite features (Figures 12, 13b), which might imply the existence of an amorphous phase whose local structure is distinct from that of metakaolinite obtained after preheating at 550°C.

Diffraction features of the intermediate phases, their contents, and interpretation

The kaolinite phases, whose 02*l*, 11*l* and 20*l*, 13*l* regions of the XRD patterns are shown in Figure 12, are named "intermediate" because their diffraction features are, on the one hand, similar to those of the untreated kaolinite and, on the other hand, display peculiarities that are unusual for

natural kaolinite varieties. Importantly, in both samples, the content of the intermediate phase, C_{inter}, decreases with $D_T(XRD)$ from 23-25% at the beginning of dehydroxylation to 2% at $D_T(XRD)$ =98% (Table 2). Moreover, the rate of the decrease in the content of untreated kaolinite in the samples, C_{in}, with increasing $D_T(XRD)$ is higher than that of the intermediate phase. In particular, the increase in $D_T(XRD)$ from 20 to 85% in KGa-1 decreases the C_{in} content from 55 to 5%, whereas, within the same range of $D_T(XRD)$, the C_{inter} content decreases only from 25 to 10% (Table2). As a result, at $D_T(XRD)$ =85%, the content of the intermediate phase (10%) is twice as high as that of untreated sample (5%). A similar regularity is observed for KGa-2 (Table 2). For this reason the metakaolinite-subtracted DRIFT features become most distinct at high D_T.

The diffraction features of the intermediate phases, to a certain extent, inherit those of the initial kaolinite structures. The most remarkable feature of the XRD patterns of the intermediate phases of both samples formed at $D_T(XRD) < 90\%$ is that they contain a nearly rational series of basal reflections with minor, irregular deviations of *l*d(*00l*) from the averaged d(*001*) (Figure 12). This means that kaolinite layers retain their fundamental one-dimensional periodicity along the c* axis and the dimensions (1:1 layer + interlayer) during the formation of the intermediate phase. Notably, the basal reflections of the intermediate phases preserve their narrow shape and relatively high intensities in comparison with those of the other *hkl* reflections. The one-dimensional periodicity along the *c** axis was lost at $D_T(XRD) > 90\%$ and $D_T(XRD) > 98\%$ of the KGa-2 and KGa-1 samples, respectively (Table 2, Figure 12). To elucidate the specific diffraction features of the intermediate phases, they were compared with those of the initial kaolinite structures of KGa-1 and KGa-2, respectively. The XRD pattern of each intermediate phase calculated by subtracting metakaolinite and the initial kaolinite (C_{in}) contents (Figure 12) was normalized to that of the untreated sample. Therefore, the actual differences between the peak intensities should be ignored while the positions are the matter of comparison. It is convenient to confine the consideration to the most diagnostic 02*l,* 11*l* and 20*l*, 13*l* regions (Figures 14 and 15).

The 20*l*, 13*l* XRD region. Two characteristic triplets of 20*l* and 13*l* reflections are especially pronounced in the intermediate phases of the KGa-1 sample (Figure 14a). Moreover, in these regions the reflections having identical indices have fairly similar positions. However, the 131 reflection of the intermediate phases is shifted to lower 2θ angles (Figure 14a). In addition, the$1\bar{3}1$ reflection of the phases formed at 425°C and 435°C is shifted toward the 131 reflection. (Figure14a). These shifts may be related to the layer displacements by the vector t_0. Figure 16a compares the positions of 20*l* and 13*l* reflections of the untreated KGa-1 sample with those observed in the XRD pattern calculated for the KGa-1 structural model in which the content of the t_0 layer displacements in the LOK component (cf. Table 1) increases from 5 to 15% at the expense of the t_2 content. The diffraction effect resulting from this new distribution of stacking faults corresponds, at least qualitatively, to the observed shift of the 131 and $1\bar{3}1$ reflections in the modeled structure (Figure 16a).

Although the number of 20*l* and 13*l* reflections of the intermediate phases and the untreated KGa-2 sample remains the same, the positions of these reflections, as well as their resolution, change significantly (Fig.14b). In particular, in the XRD patterns of the intermediate phases preheated at 410°C and 420°C the positions of the 20*l* and 13*l* reflections are shifted towards lower 2θ angles (Figure 14b). That shift most probably indicates that the *a* and *b* unit-cell parameters of the intermediate phases formed at T ≤ 430°C increase with respect to the untreated sample. Figure 17a compares two calculated XRD patterns containing 20*l*, 13*l* regions corresponding to the KGa-2 structural model having unit-cell parameters of the untreated sample and *a* = 5.170Å, *b* = 8.970Å, as in the virtual intermediate phase. The comparison of the 20*l*, 13*l* range of the intermediate phase formed at 410°C with that of the virtual phase modeled with the larger unit-cell dimensions (Figure 17b) shows that the positions of reflections with corresponding *hkl* indices are shifted to lower 2θ values. The tendency for the systematic shift of the XRD reflections position becomes less pronounced in the intermediate phases preheated at T > 420°C (Figure 14b). The reflection positions, however, show that the layer stacking sequences in the intermediate phases of both

samples are determined mostly by the layer displacement vectors t_1, t_2, and t_0. The directions and absolute values of these vectors may slightly change due to the structural modification of layers of the intermediate phases. Nevertheless, there is a certain correlation between the experimental positions of 20*l* and 13*l* reflections of the intermediate phases and those corresponding to either the initial samples or the modified models with introduced additional stacking faults that may have appeared during the formation of the intermediate phases(Figure 14a,b).

The 02*l*, 11*l* XRD region. The main modifications of the diffraction features in the XRD patterns of the intermediate phases are observed in the *02l, 11l* region (Figure15a,b). First, the intensity of the 020 reflection of the intermediate phases decreases progressively and becomes negligible after preheating of KGa-2 and KGa-1 at 430°C and 460°C, respectively. At these temperatures, the layers of the intermediate phases practically lose their two-dimensional periodicity. In agreement with the shift of the 20*l* and 13*l* reflections of the intermediate phases of the KGa-2 sample preheated at 410°C and 420°C (Figure 17), the *020* reflection of the intermediate phases is shifted to lower 2θ angles with respect to the untreated sample (Figure 15b), which implies an increase in the unit-cell *b*-parameter of these phases. Second, the diffuse maximum located close to the 020 reflection at about 20.2°2θin the XRD pattern of the untreated KGa-2 sample is transformed into a strong bell-shaped diffuse band within 20.2-21.8°2θ, with a maximum at ~20.8°2θ (Figure15b). These results imply that the intermediate phases preheated at 430°C and 440°C preserve some structural periodicity along the *c** axis, as well as within the individual layers. Therefore, the intensity modifications observed in the 11*l*, 02*l* region are most probably related to the distortions in the octahedral sheets of the intermediate phases due to possible partial dehydroxylation, violation of the six-fold coordination around some Al cations, and a re-arrangement of the atomic positions.

XRD patterns of the KGa-1 intermediate inherit some diffraction features of the initial HOK and LOK phases (Figure 15a, cf. Figure 2). Each of these phases, therefore, seems to have a particular pathway to form its unique intermediate components that are hereafter referred to as HOK and LOK intermediate components, respectively. It is natural to assume that the structural evolution

and diffraction features of the intermediate LOK components formed during partial dehydroxylation of the KGa-1 sample are similar to those of the KGa-2 sample. Indeed, the main structural features of the LOK phase and KGa-2 sample in their untreated state are quite similar (Table 1). In contrast, the evolution of the HOK intermediate components starts at higher temperatures than those of LOK; for example, the profile and positions of the HOK component formed at 425°C are similar to those of the untreated HOK phase (Figure 15a).

Another characteristic feature of the HOK components is that the maximum of the overlapping $1\bar{1}0$ and 110 reflections is shifted toward higher 2θ angles with respect to the corresponding peak of the untreated HOK phase (Figure 15a). Figure 16d compares the XRD pattern of the untreated sample with a structural model of the HOK component where the content of the $\mathbf{t_2}$ layer displacements increases from 3% to 23%. As expected, this structural modification shifts significantly the maximum of the $1\bar{1}0$ and 110 reflections toward higher 2θ angles, whereas 020 and overlapping $11\bar{1}$ and $1\bar{1}\bar{1}$ reflections almost preserve their positions (Figure 16d). Moreover, the introduction of the high content of the $\mathbf{t_2}$ translations does not affect the positions of 20*l* and 13*l* reflections (Figure 16c). Therefore, a shift of the $1\bar{1}0$ and 110 reflections toward higher 2θ angles observed in the KGa-1 HOK components most probably results from the formation of the $\mathbf{t_2}$ layer displacements at the expense of the decreasing amount of the $\mathbf{t_1}$ layer displacement.

Third, in the XRD patterns of the HOK components preheated at T > 425°C, a new effect is observed: the $1\bar{1}0$, 110 and $1\bar{1}\bar{1}$, $11\bar{1}$ reflections are merged into a single broad and intense diffuse scattering region (Figure 15a). Moreover, at a qualitative level, the XRD patterns of the intermediate phases of the KGa-1 preheated at 460°C (Figure 15a) and 510°C (Figure 11) resemble those of KGa-2 preheated at 430°C and 440°C(Figure 15b). Such similarity may result from two tendencies in the evolution of the HOK intermediate components: (a) increasing structural disorder due to the formation of enantiomorphic structural fragments resulting from the additional t_2 layer displacements and probably from random stacking faults; (b) the progressive structural

transformation of individual layers of HOK components due to partial dehydroxylation leading to a progressive distortion of the octahedral sheets. At $D_{T(XRD)} > 85\%$, these two trends in the KGa-1 may result in the formation of a single intermediate phase.

Remarkably, the existence of the HOK and LOK components in the intermediate phases of sample KGa-1 is crucial for the explanation of the specific diffraction features observed in the 02*l*, 11*l* and 20*l*, 13*l* XRD regions. Indeed, each of these components proved to have different sensitivity of the above XRD regions to different types of stacking faults. Thus the introduction of the $\mathbf{t_0}$ layer translation affects the positions of the 20*l*, 13*l* reflections (Figure 16a) but has no effect on those of the 02*l*, 11*l* reflections (Figure 16b). In contrast, the introduction of $\mathbf{t_2}$ translations selectively shifts some of the 02*l*, 11*l* reflections (Figure 16d) and preserves the positions of the 20*l*, 13*l* reflections (Figure 16c).

Conclusions and implications for kaolinite pretreatment

The results obtained imply that partial dehydroxylation of kaolinite leads to a formation of the intermediate phases that represent a new type of the defective kaolinite structures. Indeed, the natural kaolinite varieties differ from each other by the types and distribution of different layer translations, whereas the composition and structure of individual 1:1 layers remain identical irrespective of the structural order-disorder (Plançon et al., 1989; Kogure and Inoue, 2005; Kogure et al., 2010, Sakharov et al., 2016). The main structural feature of the intermediate phases is that their octahedral sheets are partially dehydroxylated. The higher the degree of dehydroxylation, the higher the structural transformation of the layers forming the intermediate phases, leading to particular diffraction effects in their XRD patterns. The intermediate phase should have metastable structure, and different structural arrangements are formed depending on the initial structure of kaolinite and the actual degree of dehydroxylation. It is quite plausible that short preheating at high temperature, just above the temperature of maximum dehydroxylation, can lead to formation of

high contents of the intermediate phase; or vice versa, rehydroxylation of metakaolinite leads to the formation of the intermediate phases (Kloužková et al. 2013). The present paper presents reliable, direct techniques not only to reveal the intermediate phases in partially dehydroxylated kaolinite, samples but also estimate quantitatively their contents. Determination of the actual structure of these phases, including reliable determination of the atomic positions, however, requires further investigation.

Understanding the occurrence and structure of the kaolinite semi-dehydroxylate phase may be key to technological properties of a calcined kaolinite and to predicting particular calcination conditions for a given kaolinite sample. It is the properties of the intermediate phase that could increase thermal stability of kaolinite-based nanorolls (Yuan et al., 2013) or play a role during geopolymerization (Medri et al., 2010). The potential of kaolinite rehydroxylation for technological and archeochronological purposes can be directly linked to the formation of intermediate phases. Because of retaining the 1:1 structure intact, it is the intermediate phases that become rehydroxylated first and trigger further rehydroxylation in a particle (Rocha et al., 1990).

Acknowledgments

The study was supported by the ATLAB project financed the RegPot within of the EU 7th Framework Programme, an internal grant of the Institute of Geological Sciences, PAS, and by the budget project #0135-2014-0032 of Geological Institute, RAS. The authors are grateful to the anonymous referees for valuable comments.

References

Bailey, S.W. (1988) Polytypism of 1:1 layer silicates. In S.W.Bailey, Ed., Hydrous phyllosilicates (Exclusive of Micas), p. 9-27. Reviews in Mineralogy, Mineralogical Society of America, Chantilly, Virginia.

Bergaya, F., Dion, P., Alcover, J.-F., Clinard, C., and Thoubar, D. (1996) TEM study of kaolinite thermal decomposition by controlled-rate thermal analysis. Journal of Materials Science, 31, 5069-5075.

Bish, D.L. and von Dreele, R.B. (1989) Rietveld refinement of non-hydrogen atomic positions in kaolinite. Clays and Clay Minerals, 37, 289-296.

Brindley, G. W. and Robinson, K. (1946) The structure of kaolinite. Mineralogical Magazine, 27, 242-253.

Brindley, G.W., Kao, C.-C., Harrison, J.L., Lipsicas, M., and Raythatha, R. (1986) Relation between structural disorder and other characteristics of kaolinites and dickites. Clays and Clay Minerals, 34, 239-249.

Bookin, A.S., Drits, V.A., Plançon, A., and Tchoubar, C. (1989) Stacking faults in kaolin-group minerals in the light of real structural features. Clays and Clay Minerals, 37, 297-307.

Derkowski, A., Drits, V.A., and McCarty, D.K. (2012) Nature of rehydroxylation in dioctahedral 2:1 layer clay minerals. American Mineralogist, 97, 610-629.

Dion, P., Alcover, J.F., Bergaya, F., Ortega, A., Llewellyn, P.L., and Rouquerol, F. (1998) Kinetic study by CRTA of the dehydroxylation of kaolinite. Clay Minerals, 33, 269-276.

Djemai, A., Balan, E., Morin, G., Hernandez, G., Labbe, J.C., and Muller, J.P. (2001) Behaviour of paramagnetic iron during the thermal transformations of kaolinite. Journal of the American Ceramic Society, 84, 1017-1024.

Drits, V.A. and Tchoubar, C. (1990) X-Ray Diffraction by Disordered Lamellar Structures, 371p. Springer-Verlag, Berlin – Heidelberg - New York.

Drits, V.A. and Derkowski, A. (2015) Kinetic behavior of partially dehydroxylated kaolinite. American Mineralogist, 100, 883-896.

Drits, V.A.,Derkowski A., and McCarty, D.K. (2012) Kinetics of partial dehydroxylation in dioctahedral 2:1 layer clay minerals. American Mineralogist, 97, 930-950.

Frost, R.L., Finnie, K., Collins, B., and Vassallo, A.M. (1995) Infrared emission spectroscopy of clay minerals and their thermal transformations. In R.W. Fitzpatrik, G.J. Churchman, and T. Eggleton, Eds., The Proceedings of the 10th International Clay Conference, Adelaide, Australia, p. 219-224. CSIRO Publications, Adelaide.

Frost, R.L. and Vassallo, A.M. (1996) The dehydroxylation of the kaolinite clay minerals using infrared emission spectroscopy. Clays and Clay Minerals, 44, 635-651.

Guggenheim, S.and Koster van Groos, A.F. (1992) High-pressure differential thermal analysis (HR-DTA). 1. Dehydroxylation reaction at elevated pressures in phyllosilicates. Journal of Thermal Analysis, 38, 1701-1728.

Guggenheim, S. and Koster van Groos, A.F. (2001) Baseline studies of The Clay Mineral Society Source Clays: Thermal analysis. Clays and Clay Minerals, 49, 433-443.

He, H.P., Guo, J.G., Zhu, J.X., and Hu, C. (2003) ^{29}Si and ^{27}Al MAS NMR study of the thermal transformations of kaolinite from North China. Clay Minerals, 38, 551-559.

Kloužková, A.,Zemenová, P.,Kohoutková, M., and Kloužek, J. (2013) Hydrothermal rehydroxylation of kaolinite studied by thermal analysis. Ceramics – Silikáty, 57, 342-347.

Kogure, T. and Inoue, A. (2005) Determination of defect structures in kaolin minerals by high-resolution transmission electron microscopy (HRTEM). American Mineralogist, 90, 85-89.

Kogure, T., Johnston, C.T., Kogel, J.E., and Bish, D. (2010) Stacking disorder in a sedimentary kaolinite. Clays and Clay Minerals, 58, 63-72.

Lee, S., Kim, Y.J., and Moon, H.S. (1999) Phase transformation sequence from kaolinite to mullite investigated by an energy-filtering transmission electron microscope. Journal of the American Ceramic Society, 82, 2841-2848.

MacKenzie, K.J.D., Brown L.W.M., Meinhold, R.H., and Brown, M.E. (1983) Outstanding problems in kaolinite-mullite reaction sequence investigated by ^{29}Si and ^{27}Al solid-state nuclear magnetic resonance. I. Metakaolinite. Journal of the American Ceramic Society, 68, 293-302.

Massiot, D., Dion P., Alcover, J.F., and Bergaya, F. (1995) ^{27}Al and ^{29}Si MAS NMR study of kaolinite thermal decomposition by controlled rate thermal analysis. Journal of the American Ceramic Society, 78, 2940-2944.

Medri, V., Fabbri, S., Dedecek, J., Sobalik, Z., Tvaruzkova, Z., and Vaccari, A. (2010) Role of the morphology and the dehydroxylation of metakaolins on geopolymerization. Applied Clay Science, 50, 538–545.

Paris, M. (2014) The two aluminum sites in the ^{27}Al MAS NMR spectrum of kaolinite: Accurate determination of isotopic chemical shifts and quadrupolar interaction parameters. American Mineralogist, 99, 393-400.

Planćon, A., Giese, R.F., Snyder, R., Drits, V.A., and Bookin, A.S. (1989) Stacking faults in the kaolin-group mineral-defect structures of kaolinite. Clays and Clay Minerals, 37, 203-210.

Ptaček, P., Šoukal, P., Opravil, T., Havilica, J., and Brandštetr, J. (2011) The kinetic analysis of the thermal decomposition of kaolinite by DTG technique. Powder Technology, 204, 20-25.

Rahier H., Wullaert, B. and Van Mele, B. (2000) Influence of the degree of dehydroxylation of kaolinite on the properties of aluminosilicate glasses. Journal of Thermal Analysis and Calorimetry, 62, 417-427.

Rocha, J. (1999) Single- and -Triple-Quantum ^{27}Al MAS NMR study of the thermal transformation of kaolinite, Journal of Physical Chemistry, B103**,** 9801-9804.

Rocha, J. and Kalinowski, J. (1990) ^{29}Si and ^{27}Al magic-angle-spinning NMR studies of the thermal transformation of kaolinite. Physics and Chemistry of Minerals, 17, 179-186.

Rocha, J., Adams, J.M., and Kalinowski, J. (1990) The rehydration of metakaolinite to kaolinite: Evidence from solid-state NMR and cognate techniques. Journal of Solid State Chemistry, 89, 260-274.

Sakharov, B.A., Drits, V.A., and McCarty, D.K. (2016) Modeling of powder X-ray diffraction patterns of the Clay Minerals Society kaolinite standards: KGa-1, KGa-1b, and KGa-2. Clays and Clay Minerals (submitted).

Sperinck, S., Raiteri, P., Marks, N., and Wright, K. (2011) Dehydroxylation of kaolinite to metakaolin – a molecular dynamics study. Journal of Materials Chemistry, 21, 2118-2125.

Suitch, P.R. (1986) Mechanism for dehydroxylation of kaolinite, dickite, and nacrite from room temperature to 455^{o}C. Journal American Ceramic Society, 69, 61-65.

White, C.E., Provis, J.L., Proffen, T., Riley, D.P., and van Deventer, J.S.J. (2010a) Density functional modeling of the local structure of kaolinite subjected to thermal dehydroxylation. Journal of Physical Chemistry, A114, 4988-4996.

White, C.E., Provis, J.L., Proffen, T., Riley, D.P., and van Deventer, J.S.J. (2010b) Combining density functional theory(DFT) and pair distribution function (PDF) analysis to solve the structure of metastable materials: the case of metakaolin. Physical Chemistry Chemical Physics, 12, 3239-3245.

Yeskin, D., Koster van Gross, A.F.K., and Guggenheim, S. (1985) The dehydroxylation of kaolinite. American Mineralogist, 70,159-164.

Yuan, P., Tan, D., Annabi-Bergaya, F., Yan, W., Liu, D., and Liu, Z. (2013) From platy kaolinite to aluminosilicate nanoroll via one-step delamination of kaolinite: Effect of the temperature of intercalation. Applied Clay Science, 83-84, 68–76.

Figure captions

Figure 1. Comparison of the experimental (dotted lines) and calculated (solid lines) XRD patterns of the samples studied. The XRD patterns were calculated for the samples with the unit cell parameters of a = 5.1575Å, b = 8.9474Å, c = 7.1545Å, α = β = 90°, γ = 89.84°. Fit coefficient R_P equals 8.12% for KGa-1 and 10.8% KGa-2. "Ant" refers to anatase.

Figure 2. Upper: comparison of the portions of the experimental XRD pattern (dotted lines) with their analogues simulated (solid lines) using a sum of the XRD patterns of the calculated HOK and LOK phases of the KGa-1 sample, containing *hkl* reflections in the diagnostic 02*l*, 11*l* and 20*l*, 13*l* regions. "Ant" refers to anatase. Lower: the calculated patterns of HOK and LOK.

Figure 3. TG and DTG curves of the preheated specimens of the KGa-1 and KGa-2 samples.

Figure 4. Relationships between the temperature corresponding to the maximum rate of dehydroxylation (DTG_{max}, in °C) and the degree of dehydroxylation measured with TG, $D_T(TG)$.

Figure 5. Comparison of the experimental (black lines) and simulated (grey lines) by end-members (kaolinite and metakaolinite) summation DRIFT spectra of the preheated specimens of the KGa-1 sample. Below: the model-experiment differential curve, amplified.

Figure 6. Comparison of the experimental (black lines) and simulated (grey lines) by end-members (kaolinite and metakaolinite) summation DRIFT spectra of the preheated specimens of the KGa-2 sample. Below: the model-experiment differential curve, amplified.

Figure 7. XRD patterns of the KGa-1 and KGa-2 specimens preheated at different temperatures.

Figure 8. Comparison of the portions of the experimental XRD patterns (dotted lines) of the KGa-1 preheated specimens containing 02*l*, 11*l* (a) and 20*l*, 13*l* (b) reflections with their simulated analogues obtained by the optimized summation of the XRD patterns of the initial kaolinite and

metakaolinite (solid lines). The model-experimental differential curve is shown below each fragment.

Figure 9. Comparison of fragments of the experimental XRD patterns (dotted lines) of the KGa-2 preheated specimens containing the 02*l*, 11*l* (a) and 20*l*, 13*l* (b) reflections with their simulated analogues obtained by optimized summation of the XRD patterns of the initial kaolinite and metakaolinite (solid lines). The model-experimental differential curve is shown below each fragment.

Figure 10. Linear relationships between reflection intensities ratios, I_{002}/I_{ant}, and degrees of dehydroxylation, $D_T(XRD)$, $D_{Tn}(TG)$, and $D_T(IR)$, obtained on preheated specimens using different methods. Equations correspond to trend line (TL) linear correlations, black for KGa-1, gray for KGa-2. PL – point-connecting line shown as a specimen alteration path.

Figure 11. Metakaolinite-subtracted XRD patterns of the KGa-1 and KGa-2 specimens preheated at different temperatures

Figure 12. XRD patterns of the intermediate phases obtained by subtraction of the untreated kaolinite contribution from the metakaolinite-subtracted XRD patterns (cf. Figure 11).

Figure 13. Residual DRIFT spectra of the preheated specimens of the KGa-1 and KGa-2 samples after subtracting metakaolinite contribution based on the $D_T(IR)$ values (Table 2). End-member kaolinite and metakaolinite spectra presented for comparison.

Figure 14. Comparison of the fragments of the experimental XRD patterns of the untreated KG-1 and KGa-2 samples containing the 20*l*, 13*l* reflections (broken lines) to those of the intermediate phases formed in KGa-1(a) and KGa-2 (b) preheated at different temperatures, obtained by metakaolinite and kaolinite subtraction (solid lines; cf. Figure 12). Intensities of the experimental XRD patterns of the intermediate phases were normalized to those of the XRD

patterns of the untreated sample. Corresponding XRD fragments of the untreated KGa-1(a) and KGa-2 (b) presented above for comparison.

Figure 15. Comparison of fragments of the experimental XRD patterns of the untreated KGa-1 and KGa-2 samples containing the 02*l*, 11*l* reflections (broken lines) to those of the intermediate phases formed in KGa-1(a) and KGa-2 (b) preheated at different temperatures, obtained by metakaolinite and kaolinite subtraction (solid lines; cf. Figure 12). Intensities of the experimental XRD patterns of the intermediate phases were normalized to those of the XRD patterns of the untreated sample. Corresponding XRD fragments of the untreated KGa-1 (a) and KGa-2 (b) presented above for comparison.

Figure 16. Influence of different layer displacements on the XRD features of the HOK and LOK components of the intermediate phases of sample KGa-1: effect of the increase in the $\mathbf{t_0}$ content from 5 (broken lines) to 15% (solid lines) on (a) the 20*l*, 13*l* reflections of LOK and (b) 11*l*, 02*l* reflections of HOK; effect of the increase in the $\mathbf{t_2}$ content from 3 (broken lines) to 23% (solid lines) on (c) 20*l*, 13*l* reflections of LOK and (d) the 11*l*, 02*l* reflections of HOK (see text for details).

Figure 17. Comparison of the positions of the 20*l* and 13*l* reflections of the experimental XRD pattern of the KGa-2 sample (broken line) to (a) those calculated for the model with larger layer unit cell parameters, a = 5.1575Å, b = 8.9474Å (solid line) and to (b) those observed in the corresponding experimental fragment of the intermediate phase (solid line).

Table 1. Structural parameters of the HOK and LOK fractions of the KGa-1 and KGa-2 samples whole structural are described by the unit cell with a = 5.1575Å, b = 8.9474Å, c = 7.1545Å, α = β = 90°, and γ = 89.842°.

Sample	**KGa-1**		**KGa-2**	
Phase	**HOK**	**LOK**	**HOK**	**LOK**
t_1	-0.3682a -0.0225b	-0.3682a -0.0225b	-0.3682a -0.0225b	-0.3682a -0.0225b
t_2	-0.3500a +0.3047b	-0.3500a +0.3047b	-0.3500a +0.3047b	-0.3500a +0.3047b
t_0	- -	-0.3154a -0.3154b	- -	-0.3154a -0.3154b
W(t_1)	0.97	0.55	0.97	0.55
W(t_2)	0.03	0.35	0.03	0.35
W(t_0)	-	0.05	-	0.05
Wa	-	-	-	0.05
δ(t)	0.05c*	0.012a 0.022b 0.05c*	0.05c*	0.012a 0.022b 0.05c*
N	45	45	25	25
D (Å)	200 - 800	200 - 800	200 - 800	200 - 800
α (deg)	80	80	150	150
C(%)	24.3	75.7	3.9	96.1

Table 2. A list of the $D_T(TG)$, $D_{Tn}(TG)$, $D_T(IR)$, $D_T(XRD)$, and DTG_{max} values and the contents of the initial kaolinite, C_{in}, and the intermediate phases, C_{inter}, in the specimens of the KGa-1 and KGa-2 samples, preheated at different temperature, T.

T [^{o}C]	D_T(TG) [%]	D_{Tn}(TG) [%]	D_T(IR)\ [%]	D_T(XRD) [%]	C_{in} [%]	C_{inter} [%]	DTG_{max} [^{o}C]	I_{002}/I_{an}
KGa-1								
425	15.4	18.2	22	20	55	25	516	10.0
435	43.9	46.2	60	56	28	16	537	6.1
450	65.5	68.9	81	79	10	11	557	3.0
460	74.5	78.3	87	85	5	10	576	2.2
510	89.1	93.7	96	98	0	2	640	0.3
600	95.1	100	100	100	0	0	740	-
KGa-2								
410	8.9	9.7	3	5	72	23	496	3.85
420	26.5	28.8	33	28	56	16	494	3.85
430	65.5	71.1	76	78	12	10	502	2.56
440	74.7	81.1	83	89	2	9	521	0.84
470	85.9	93.3	99	98	0	0	590	0.45
550	92.1	100	100	100	0	0	667	-

Figure 1

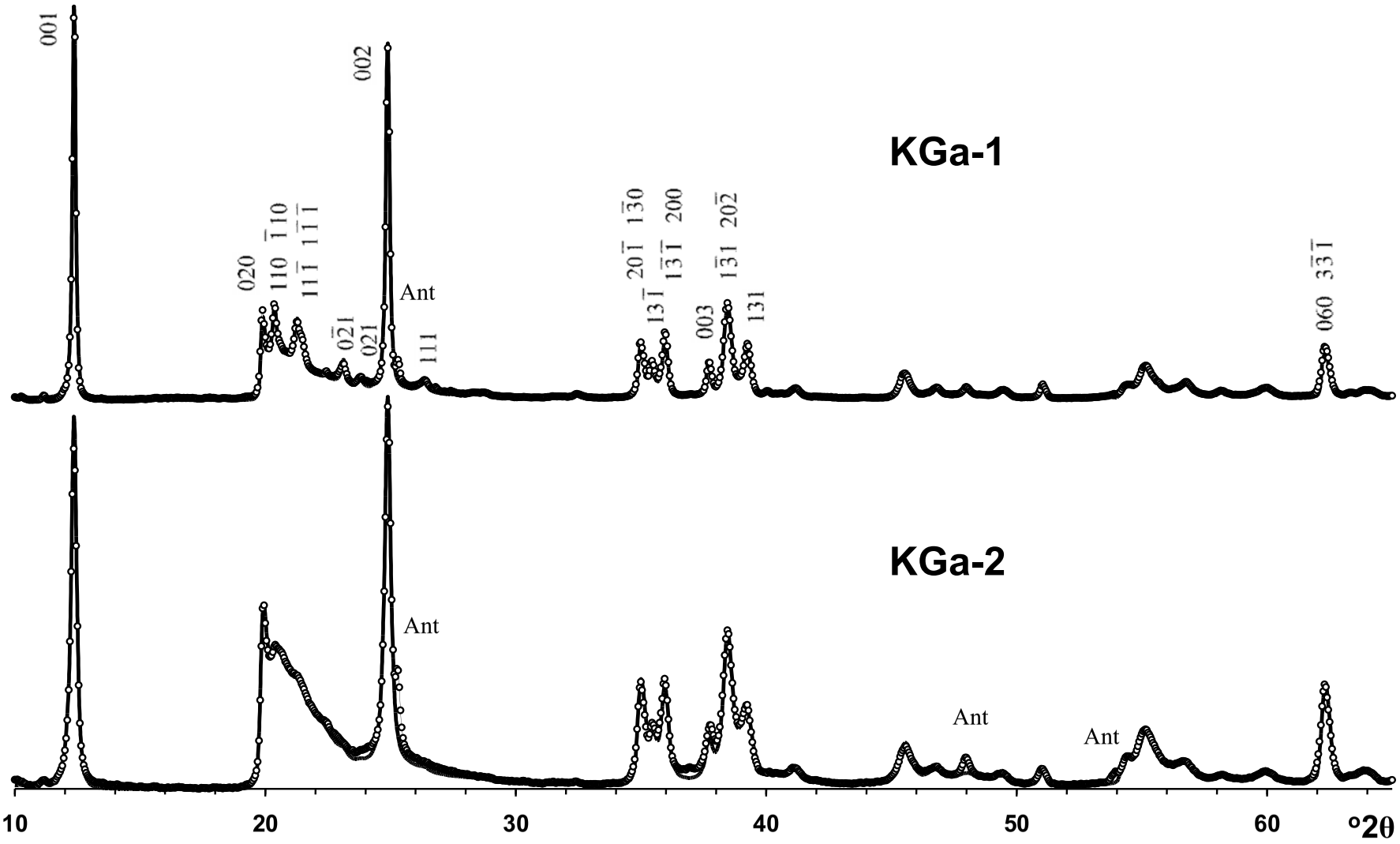
001
020
110
$\bar{1}10$
$11\bar{1}$
$\bar{1}1\bar{1}$
$0\bar{2}1$
021
002
Ant
111
$20\bar{1}$
$1\bar{3}0$
$13\bar{1}$
$\bar{1}3\bar{1}$
200
003
$1\bar{3}1$
$20\bar{2}$
131
$06\bar{0}$
$33\bar{1}$
KGa-1
KGa-2
Ant
Ant
Ant
10
20
30
40
50
60
°2θ

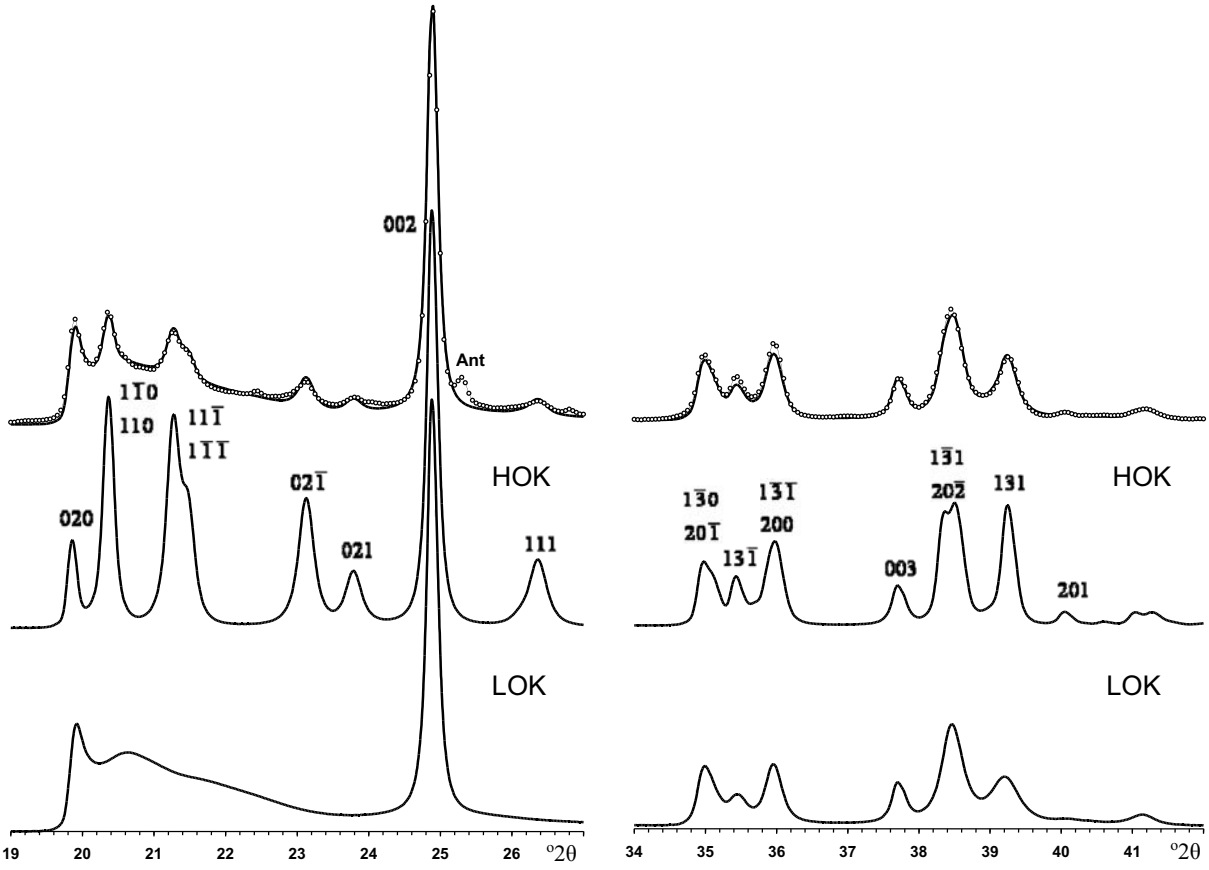
002
Ant
1$\bar{1}$0
110
11$\bar{1}$
1$\bar{1}$1
020
02$\bar{1}$
021
111
HOK
LOK
1$\bar{3}$0
20$\bar{1}$
13$\bar{1}$
1$\bar{3}$$\bar{1}$
200
003
20$\bar{2}$
1$\bar{3}$1
131
201
HOK
LOK
19
20
21
22
23
24
25
26
°2θ
34
35
36
37
38
39
40
41
°2θ

Figure 2

KGa-1

heating *T*	D_T (*TG*)
T ≈ 400°C	3.1 %
T ≈ 425°C	15.4 %
T ≈ 435°C	43.9 %
T ≈ 450°C	65.5 %
T ≈ 460°C	74.3 %
T ≈ 510°C	89.1 %
T ≈ 600°C	95.1 %

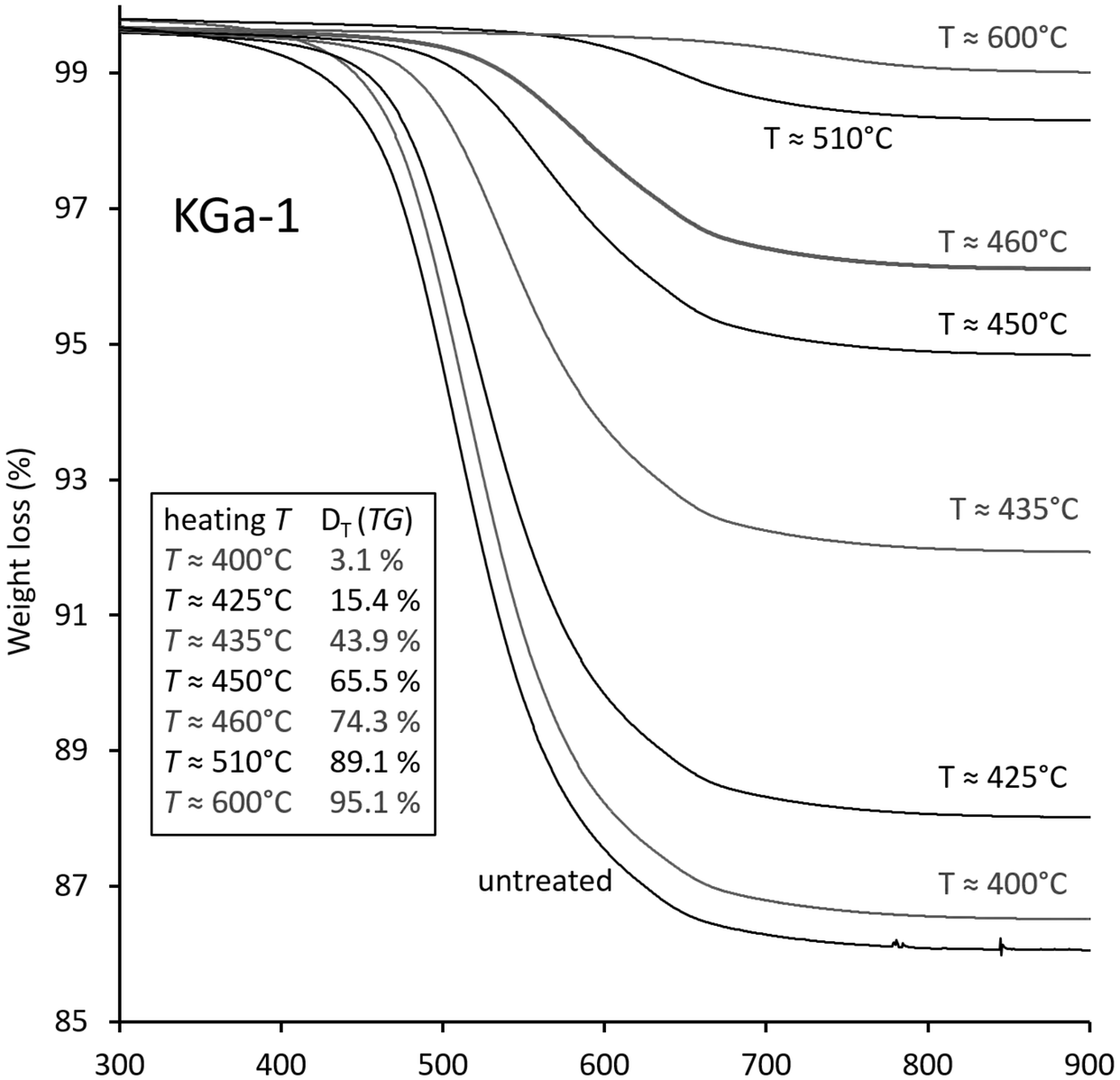

KGa-2

heating *T*	D_T (*TG*)
T ≈ 380°C	3.8 %
T ≈ 410°C	8.9 %
T ≈ 420°C	26.5 %
T ≈ 430°C	65.5 %
T ≈ 440°C	74.7%
T ≈ 470°C	85.9 %
T ≈ 550°C	92.1 %

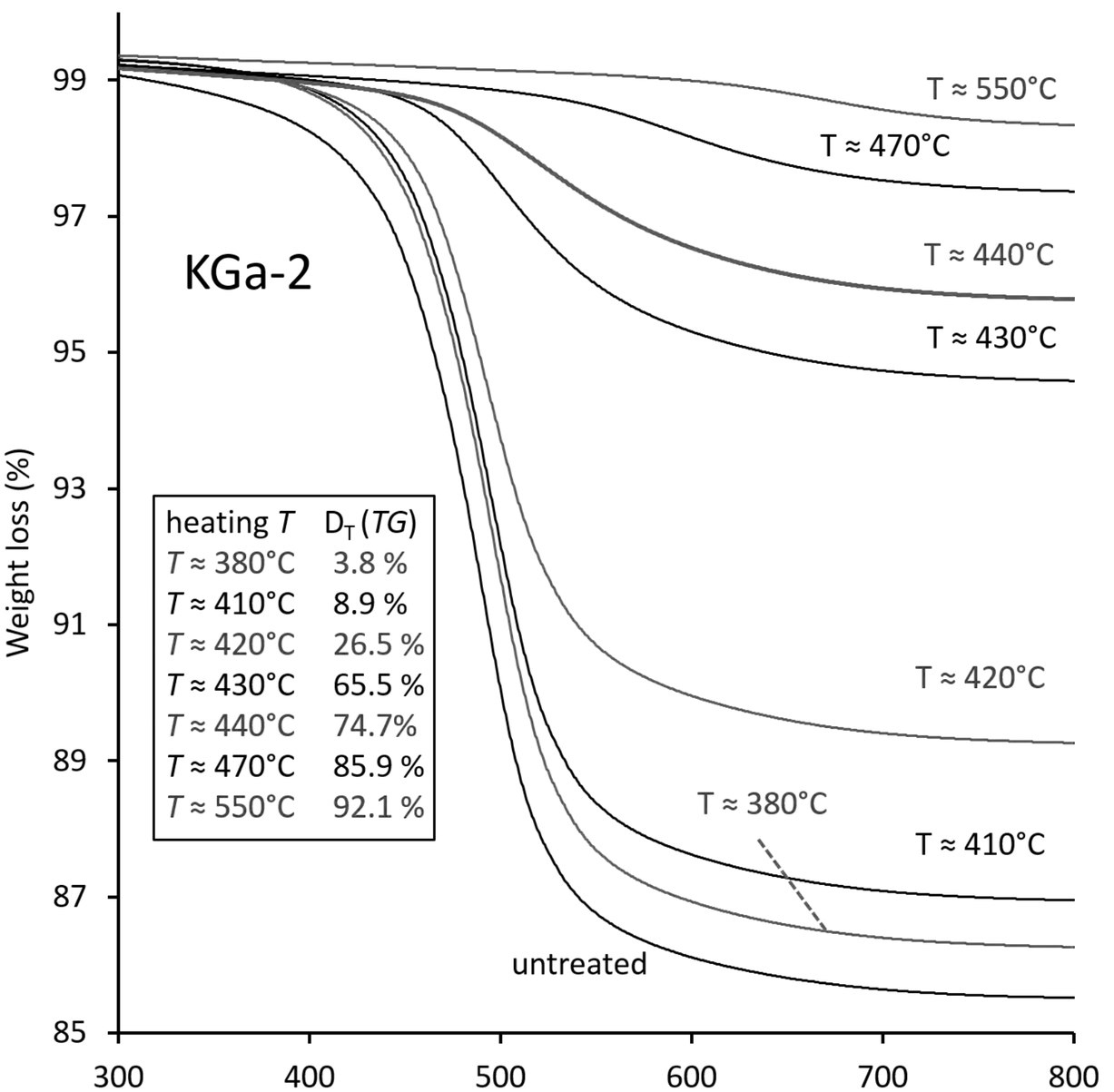

heating *T*	DTG_{max}
untreated	512 °C
T ≈ 400°C	515 °C
T ≈ 425°C	516 °C
T ≈ 435°C	537 °C
T ≈ 450°C	557 °C
T ≈ 460°C	576 °C
T ≈ 510°C	640 °C
T ≈ 600°C	740 °C

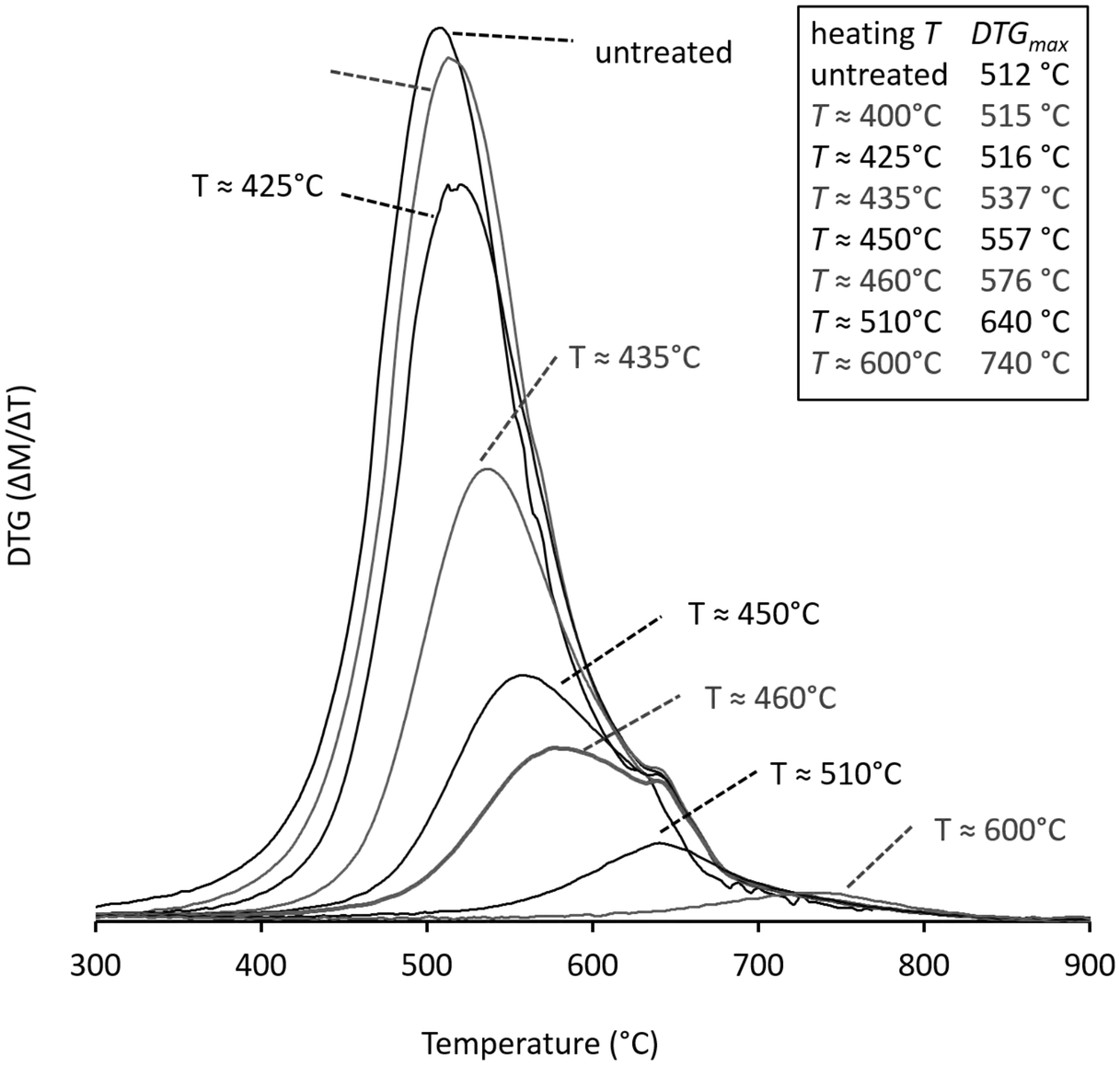

heating *T*	DTG_{max}
untreated	492 °C
T ≈ 380°C	496 °C
T ≈ 410°C	496 °C
T ≈ 420°C	494 °C
T ≈ 430°C	502 °C
T ≈ 440°C	521 °C
T ≈ 470°C	590 °C
T ≈ 550°C	667 °C

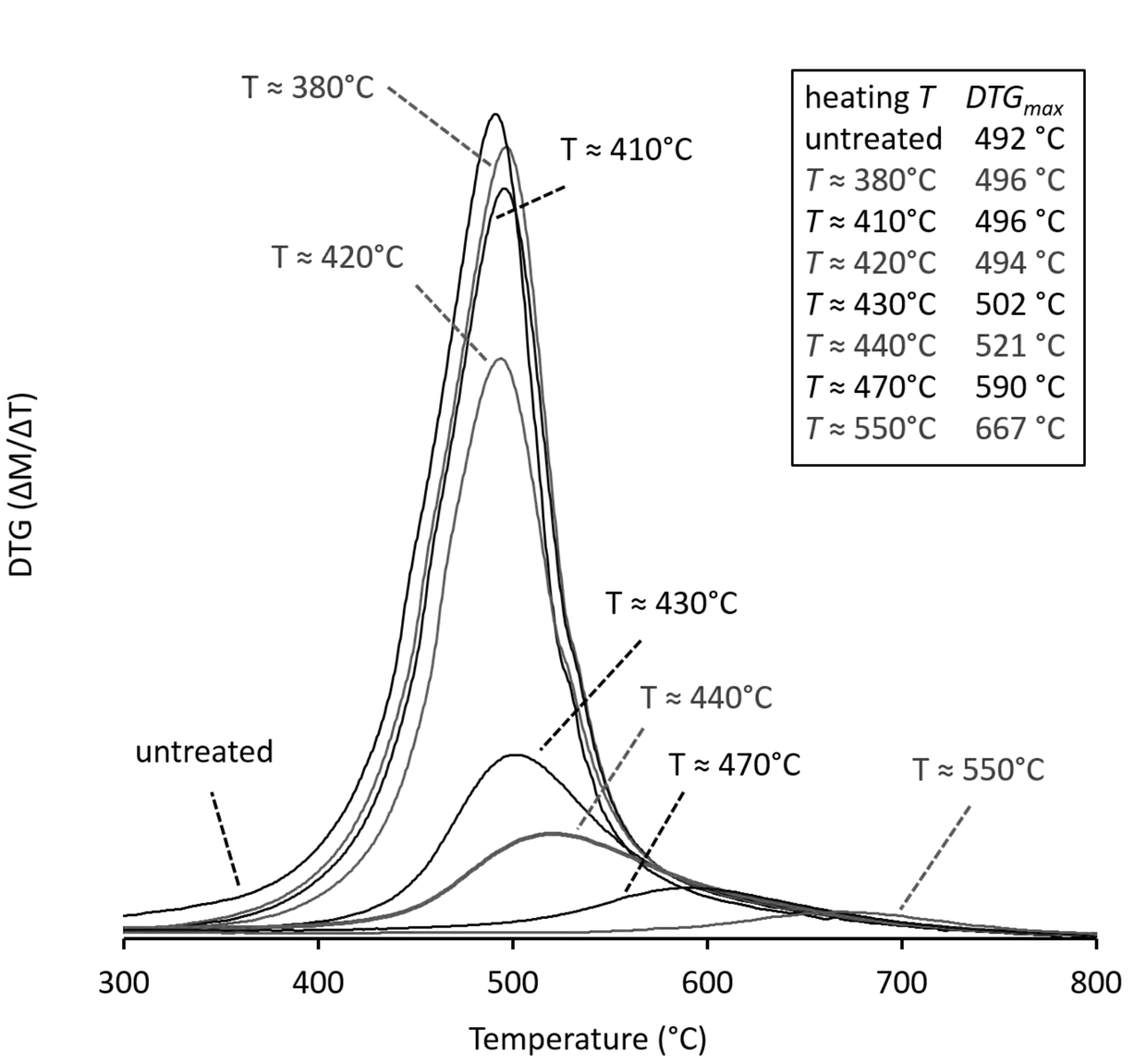

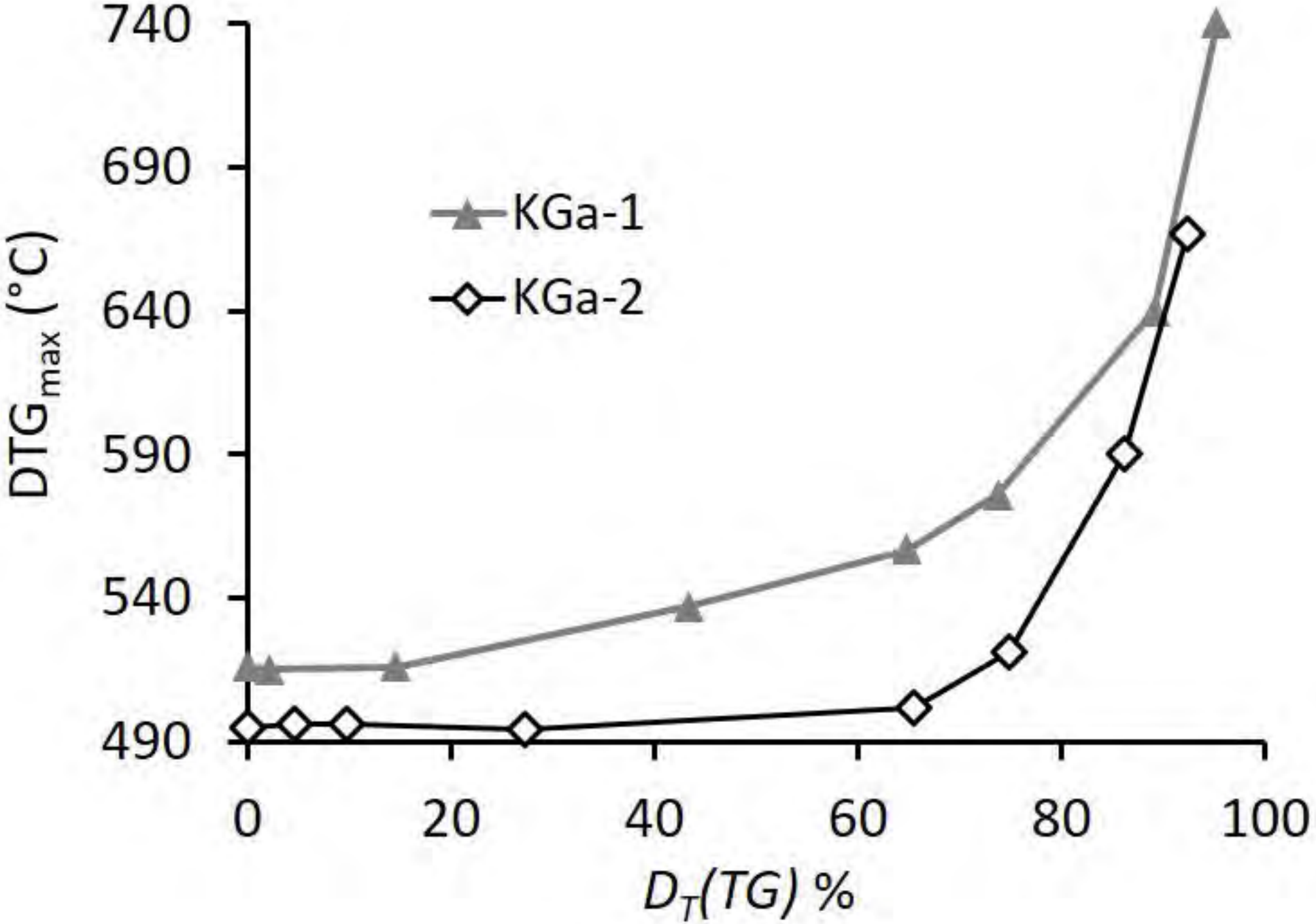
740
690
640
590
540
490
DTG$_{max}$ (°C)
KGa-1
KGa-2
0
20
40
60
80
100
$D_T(TG)$ %

KGa-1

D_T (*IR*)

0 %
2 %
22 %
60 %
81 %
87 %
96 %
100 %

T

untreated
400°C
425°C
435°C
450°C
460°C
510°C
600°C

D_T (*IR*)

2 %
22 %
60 %
81 %
87 %
96 %
100 % (assumed)

3730 3680 3630 3580 1300 1200 1100 1000 900 800 700 600 500

wavenumber (cm^{-1})

400°C
425°C
435°C
450°C
460°C
510°C

3730 3680 3630 3580 1300 1200 1100 1000 900 800 700 600 500

wavenumber (cm^{-1})

KGa-2

D_T (*IR*)

0 %

2 %

3 %

33 %

76 %

83 %

99 %

100 %

T

untreated

380°C

410°C

420°C

430°C

440°C

470°C

550°C

D_T (*IR*)

2 %

3 %

33 %

76 %

83 %

99 %

100 % (assumed)

3730 3680 3630 3580 1300 1200 1100 1000 900 800 700 600 500

wavenumber (cm^{-1})

380°C

410°C

420°C

430°C

440°C

470°C

3730 3680 3630 3580 1300 1200 1100 1000 900 800 700 600 500

wavenumber (cm^{-1})

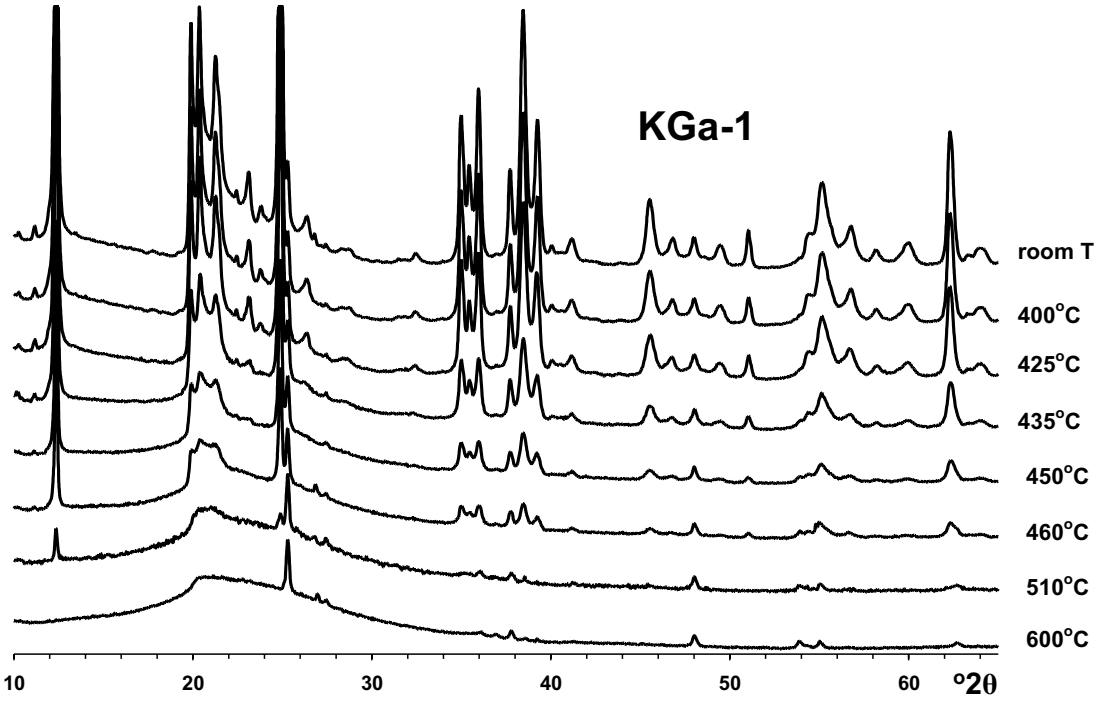
KGa-1
room T
400°C
425°C
435°C
450°C
460°C
510°C
600°C
10
20
30
40
50
60
°2θ

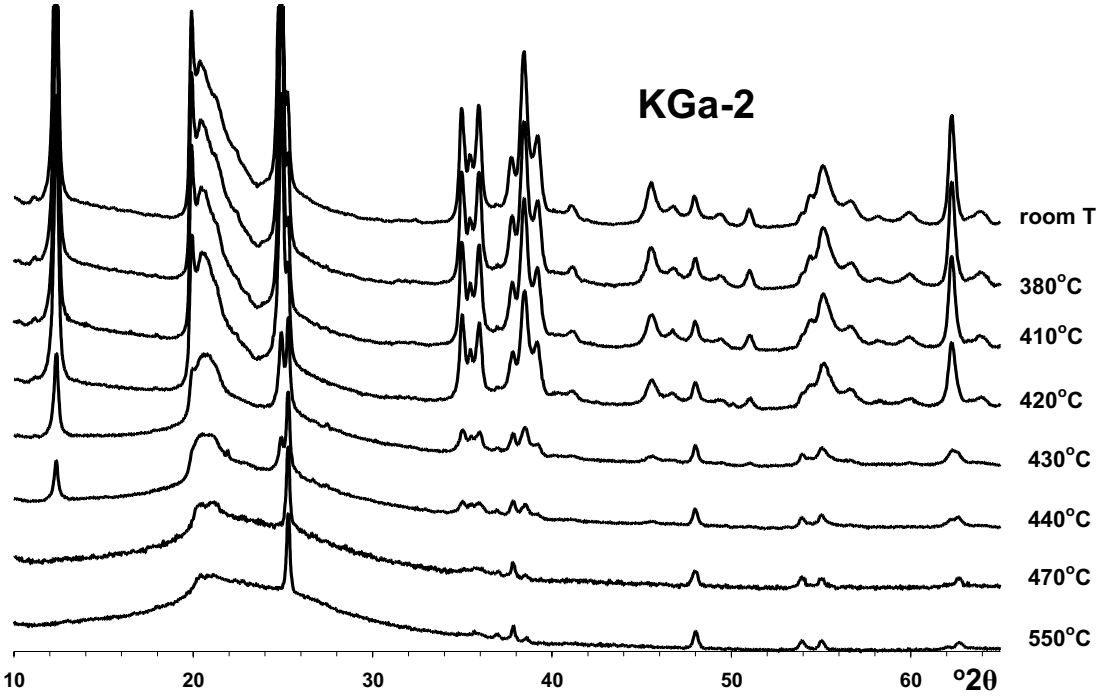
KGa-2
room T
380°C
410°C
420°C
430°C
440°C
470°C
550°C
10
20
30
40
50
60
°2θ

Figure 7

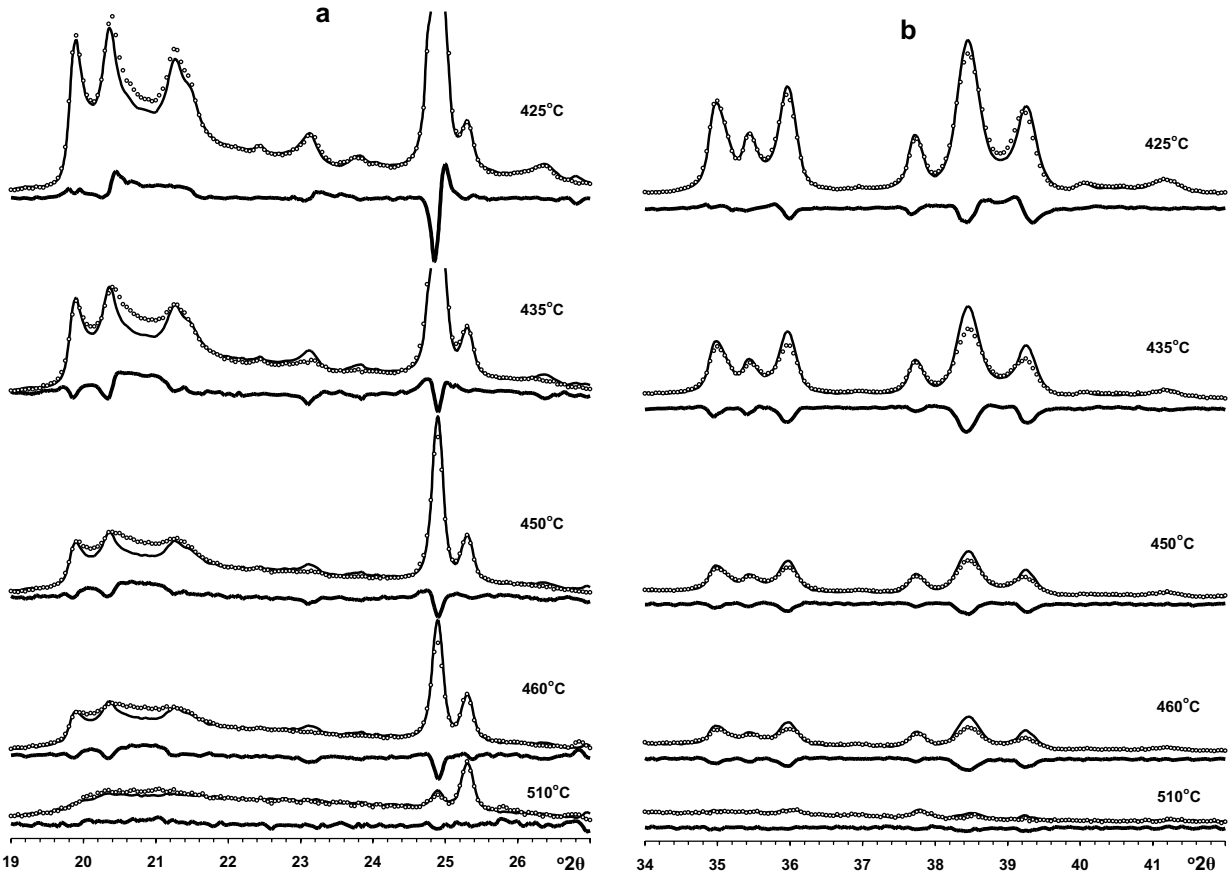
a
425°C
435°C
450°C
460°C
510°C
19
20
21
22
23
24
25
26
°2θ
b
425°C
435°C
450°C
460°C
510°C
34
35
36
37
38
39
40
41
°2θ

Figure 8

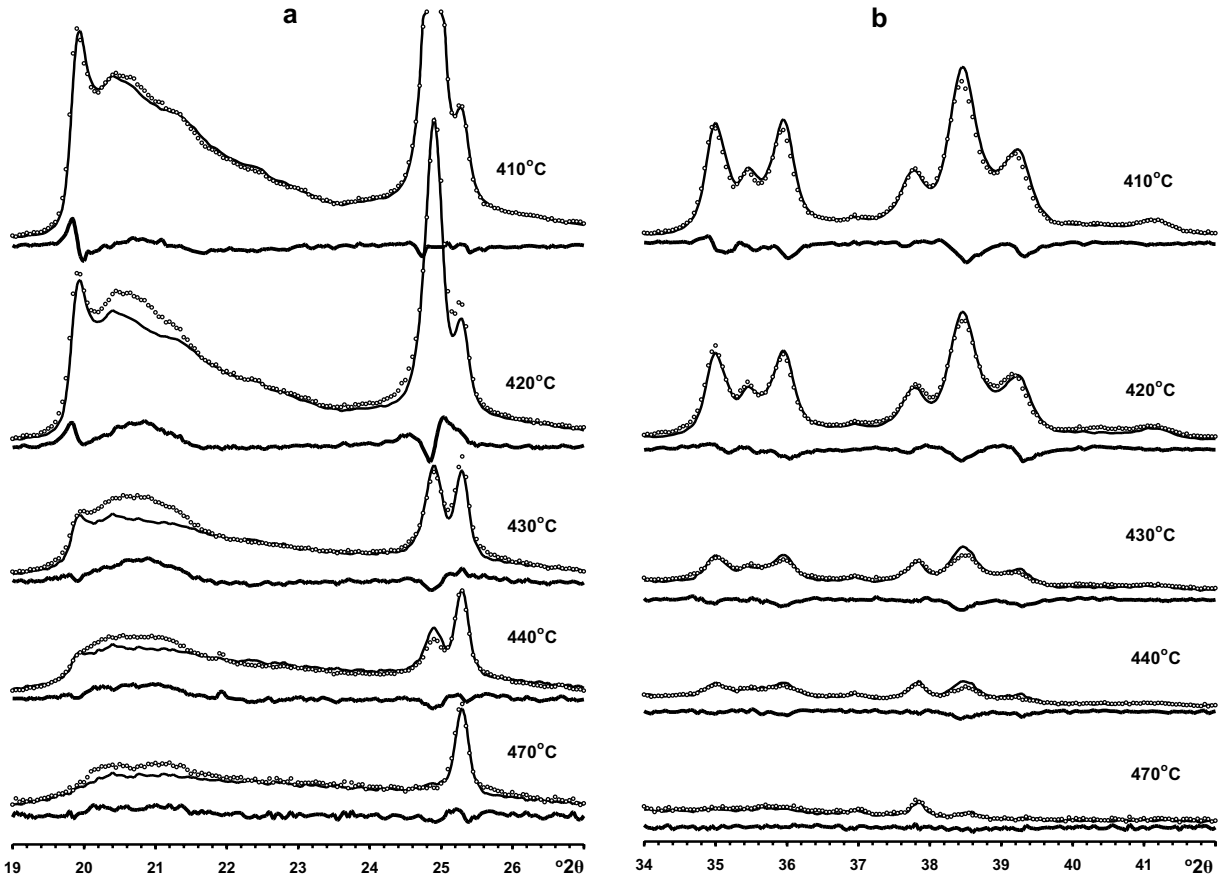
a
410°C
420°C
430°C
440°C
470°C
19
20
21
22
23
24
25
26
°2θ
b
410°C
420°C
430°C
440°C
470°C
34
35
36
37
38
39
40
41
°2θ

Figure 9

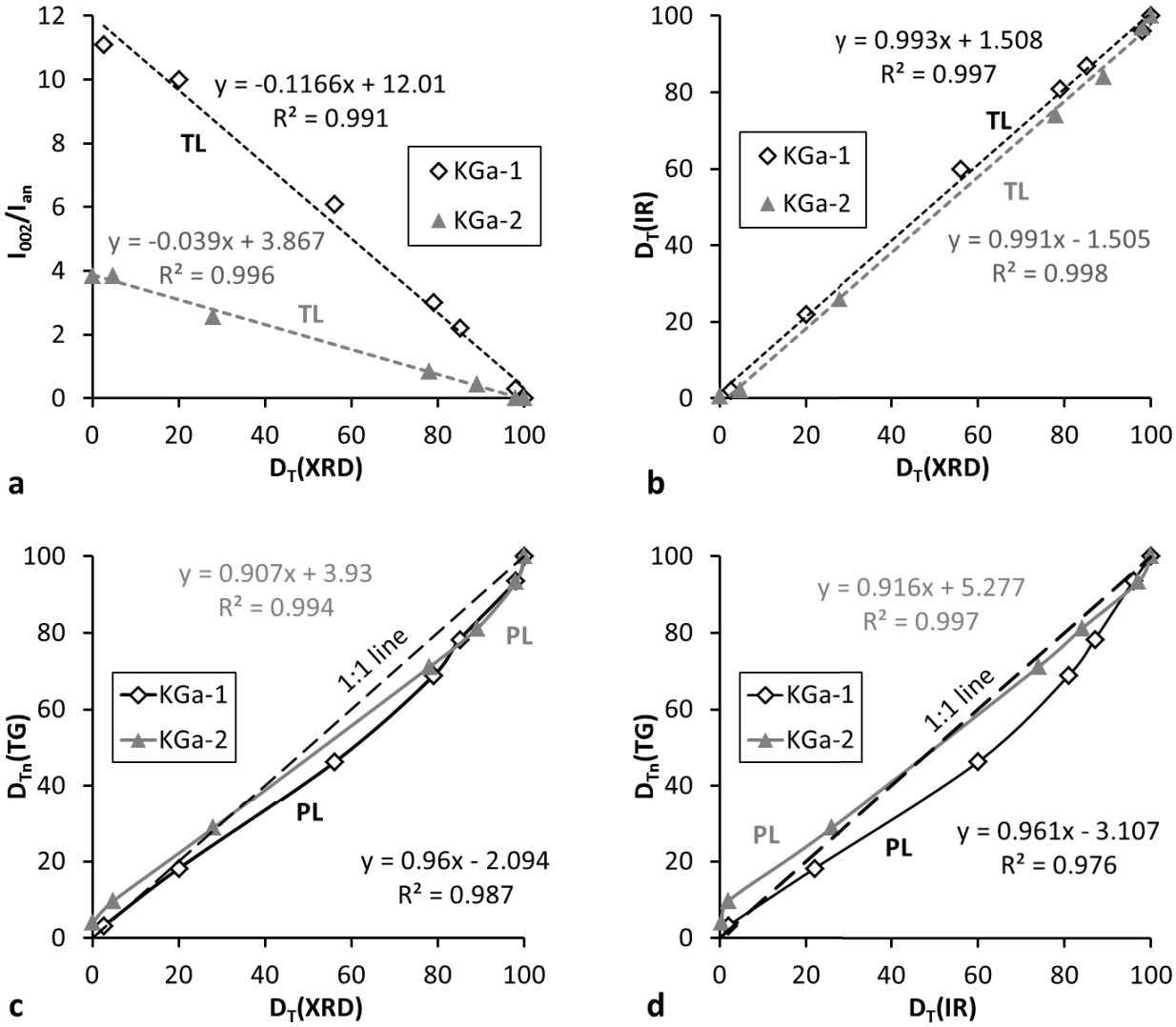
a
I_{002}/I_{an}
y = -0.1166x + 12.01
R² = 0.991
TL
y = -0.039x + 3.867
R² = 0.996
TL
KGa-1
KGa-2
D_T(XRD)
b
y = 0.993x + 1.508
R² = 0.997
TL
TL
y = 0.991x - 1.505
R² = 0.998
KGa-1
KGa-2
D_T(IR)
D_T(XRD)
c
y = 0.907x + 3.93
R² = 0.994
1:1 line
PL
PL
y = 0.96x - 2.094
R² = 0.987
KGa-1
KGa-2
D_{Tn}(TG)
D_T(XRD)
d
y = 0.916x + 5.277
R² = 0.997
1:1 line
PL
PL
y = 0.961x - 3.107
R² = 0.976
KGa-1
KGa-2
D_{Tn}(TG)
D_T(IR)

Figure 10.

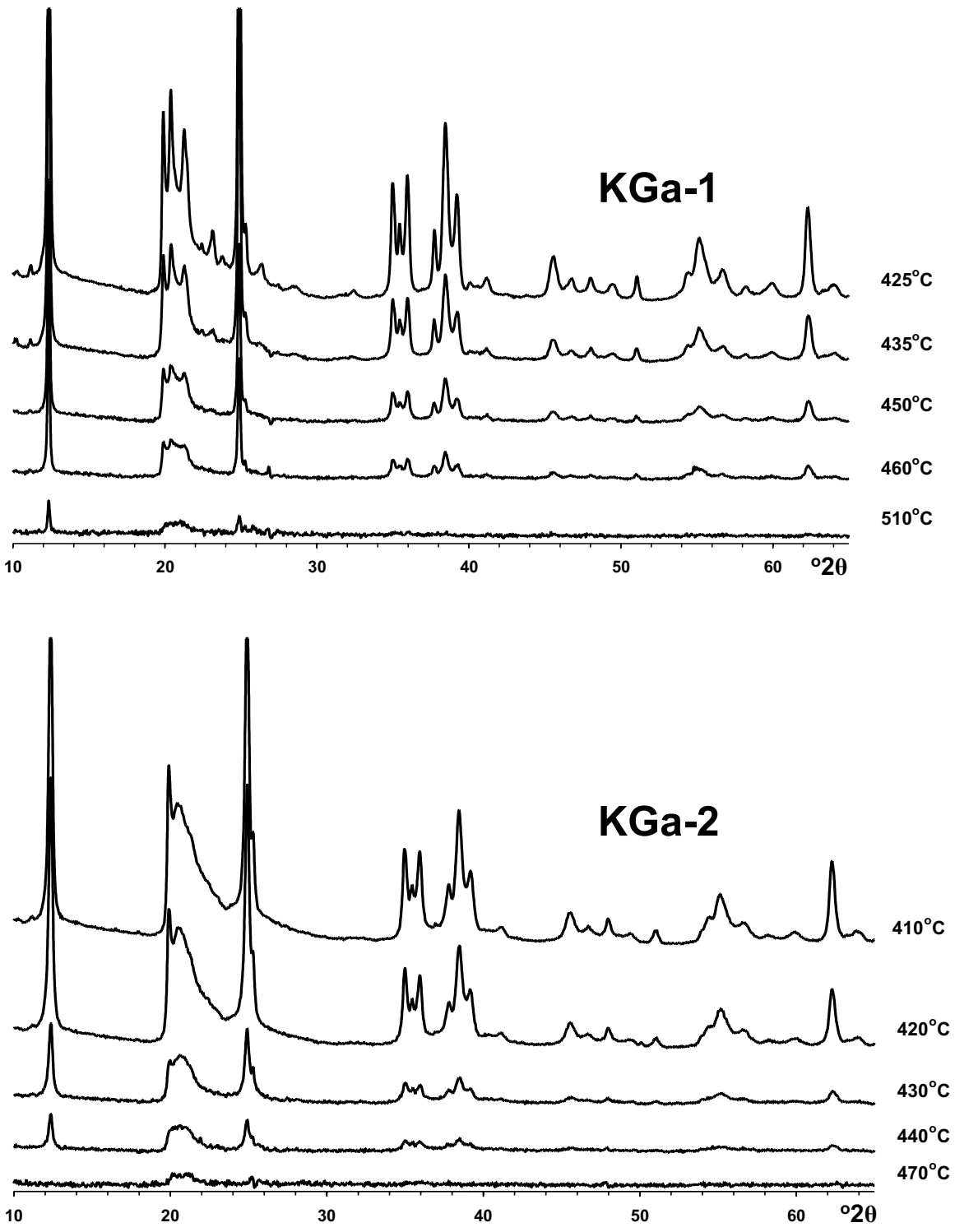
KGa-1
425°C
435°C
450°C
460°C
510°C
10
20
30
40
50
60
°2θ
KGa-2
410°C
420°C
430°C
440°C
470°C
10
20
30
40
50
60
°2θ

Figure 11

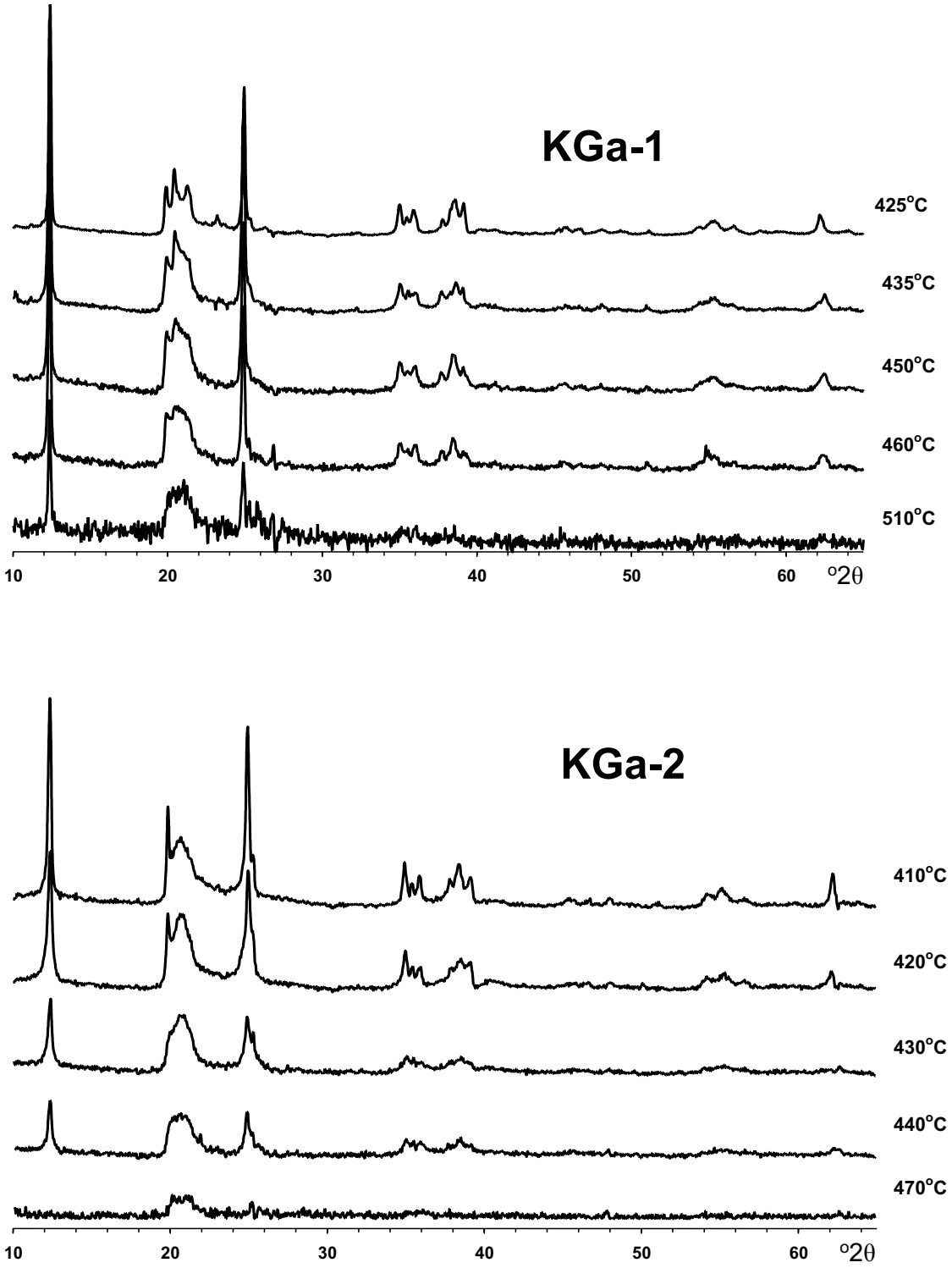
KGa-1
425°C
435°C
450°C
460°C
510°C
10
20
30
40
50
60
°2θ
KGa-2
410°C
420°C
430°C
440°C
470°C
10
20
30
40
50
60
°2θ

Figure 12

KGa-1 (metakaolinite-subtracted)

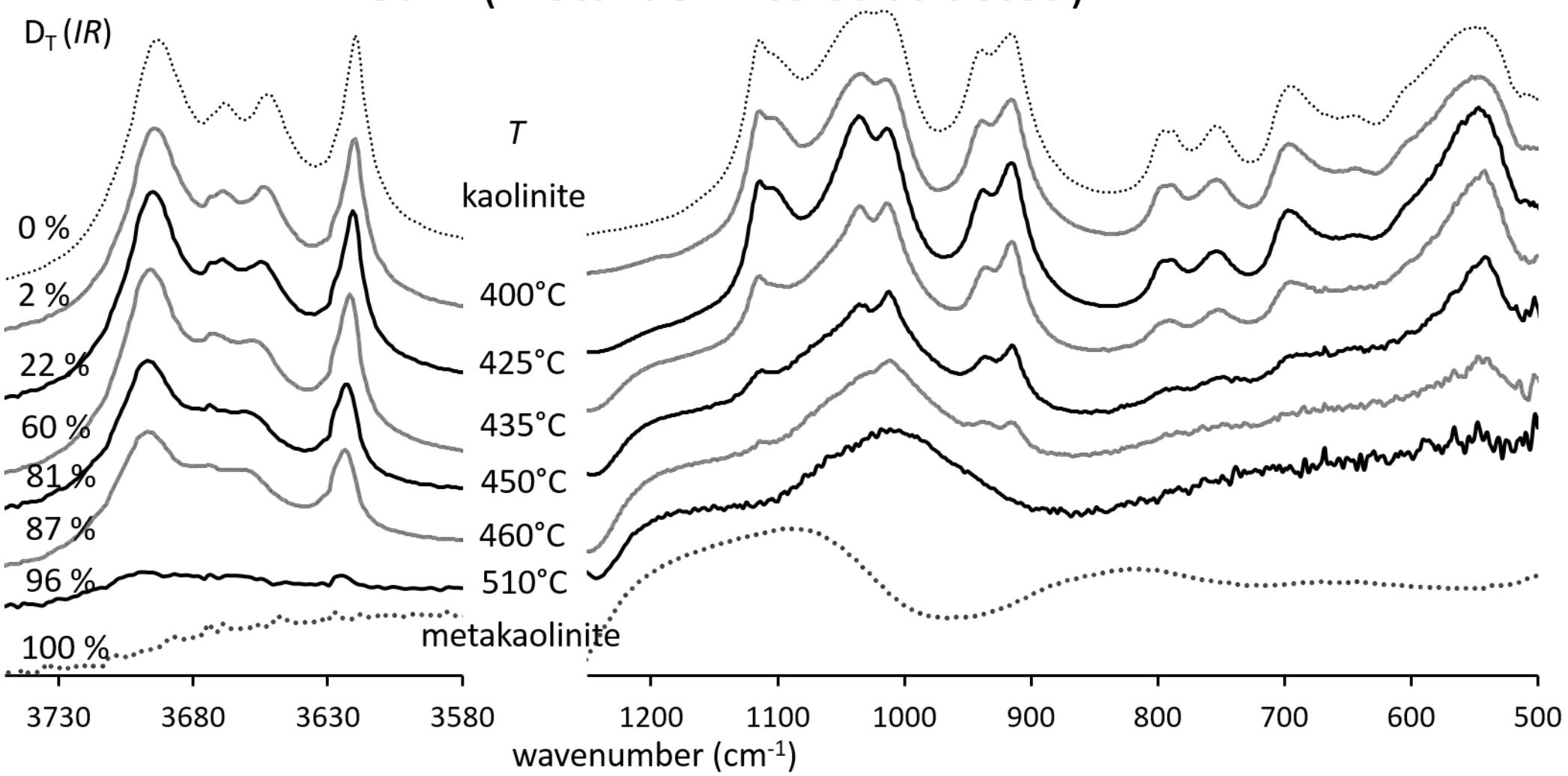

KGa-2 (metakaolinite-subtracted)

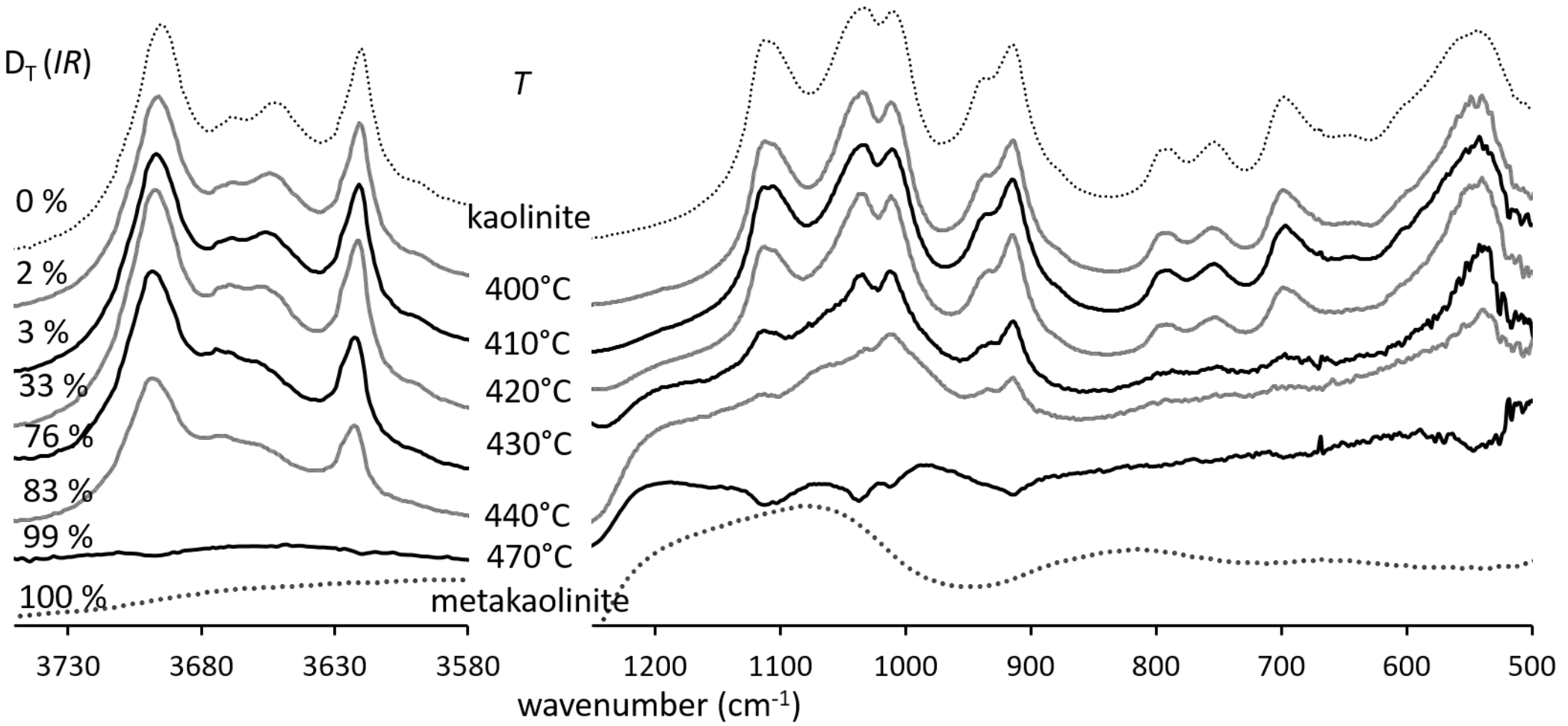

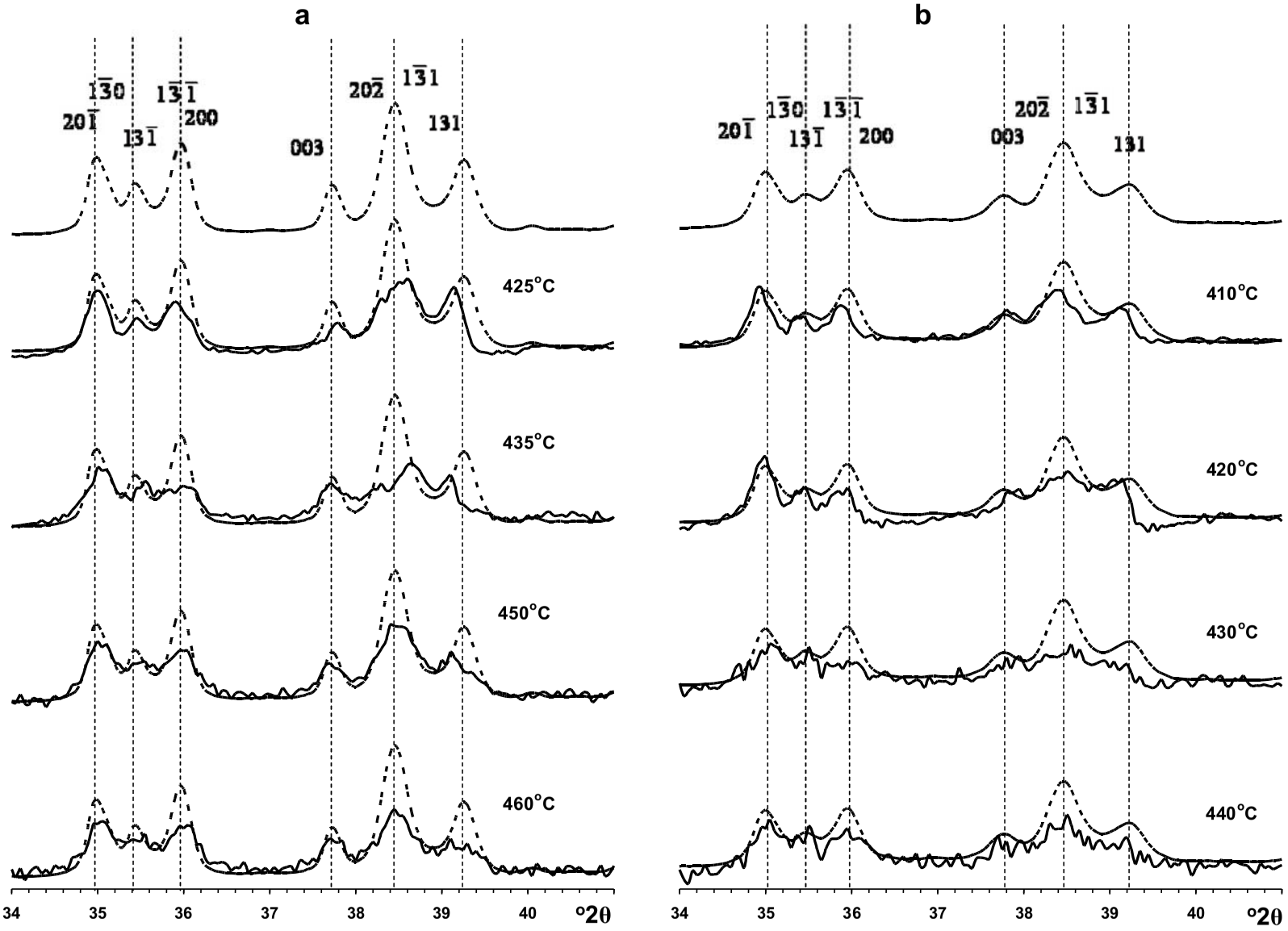
a
b
20$\bar{1}$
1$\bar{3}$0
13$\bar{1}$
131
1$\bar{3}$$\bar{1}$
200
003
20$\bar{2}$
1$\bar{3}$1
425°C
435°C
450°C
460°C
410°C
420°C
430°C
440°C
34
35
36
37
38
39
40
°2θ

Figure 14

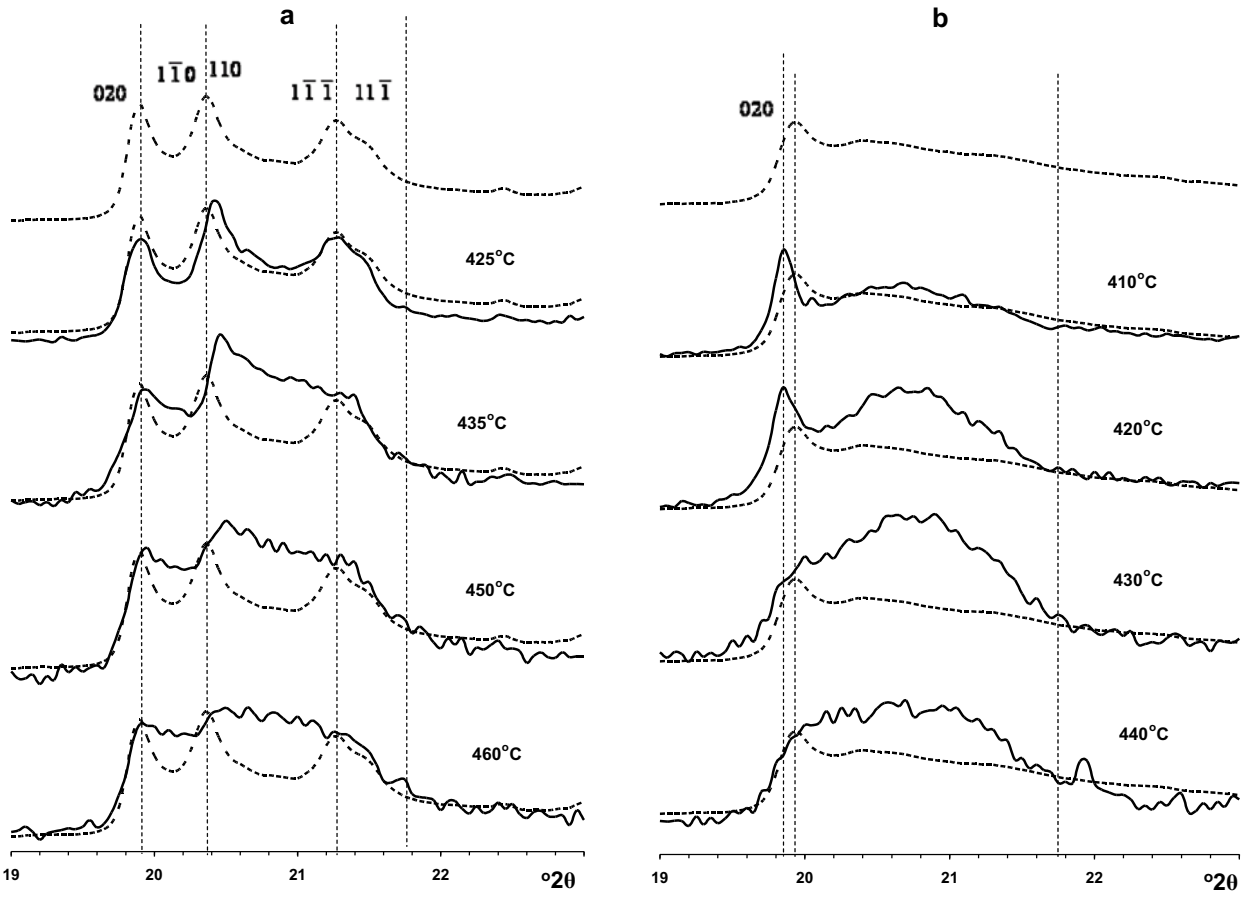
a
020
1$\bar{1}$0
110
1$\bar{1}\bar{1}$
11$\bar{1}$
425°C
435°C
450°C
460°C
19
20
21
22
°2θ
b
020
410°C
420°C
430°C
440°C
19
20
21
22
°2θ

Figure 15

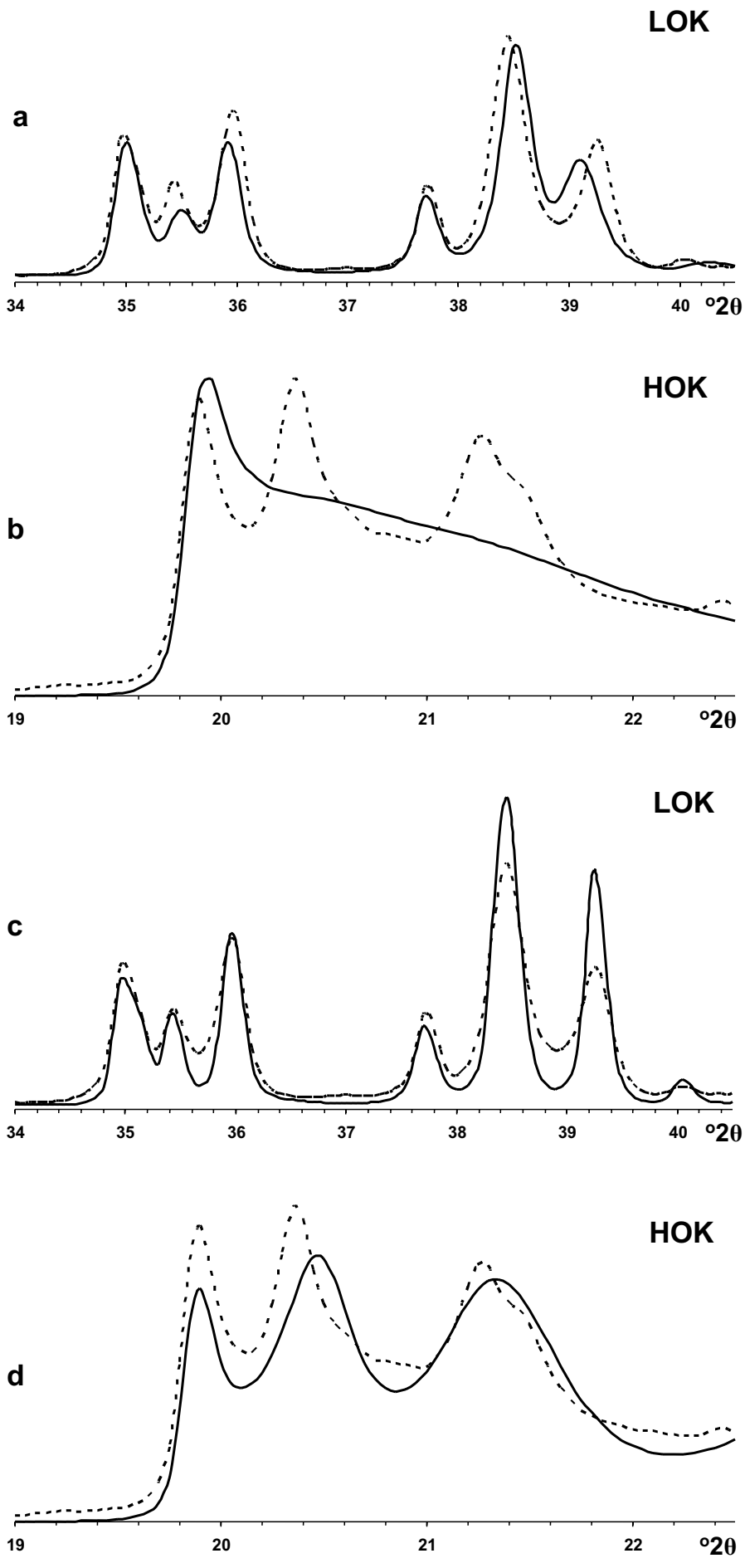
LOK
a
34
35
36
37
38
39
40
°2θ
HOK
b
19
20
21
22
°2θ
LOK
c
34
35
36
37
38
39
40
°2θ
HOK
d
19
20
21
22
°2θ

Figure 16

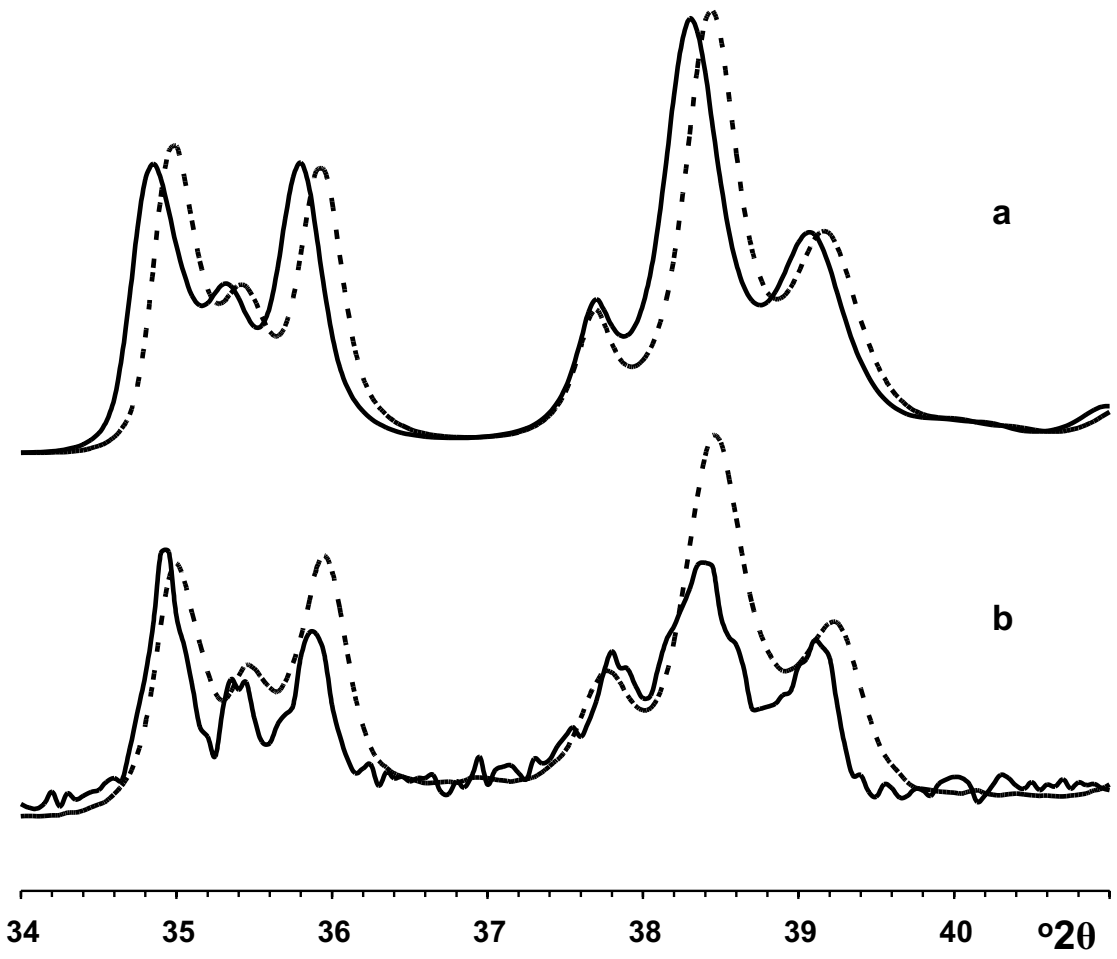

Figure 17